

# Supervised Fuzzy-Logic Classification of Hydrometeors Using C-Band Weather Radars

Frank Silvio Marzano, *Senior Member, IEEE*, Daniele Scaranari, and Gianfranco Vulpiani, *Member, IEEE*

**Abstract**—A model-based fuzzy-logic method for hydrometeor classification using C-band polarimetric radar data is presented and discussed. Membership functions of the fuzzy-logic algorithm are designed for best fitting simulated radar signatures at C-band. Such signatures are derived for ten supervised hydrometeor classes by means of a fully polarimetric radar scattering model. The Fuzzy-logic Radar Algorithm for Hydrometeor Classification at C-band (FRAHCC) is designed to use a relatively small set of polarimetric observables, i.e., copolar reflectivity and differential reflectivity, but a version of the algorithm based on the use of specific differential phase is also numerically tested and documented. The classification methodology is applied to volume data coming from a C-band two-radar network that is located in north Italy within the Po valley. Numerical and experimental results clearly show the improvements of hydrometeor classification, which were obtained by using FRAHCC with respect to the direct use of fuzzy-logic-based algorithms that are specifically tuned for S-band radar data. Moreover, the availability of two C-band rainfall observations of the same event allowed us to implement a path-integrated attenuation correction procedure, based on either a composite radar field approach or a network-constrained variational algorithm. The impact of these correction procedures on hydrometeor classification is qualitatively discussed within the considered case study.

**Index Terms**—C-band weather radar, fuzzy-logic method, hydrometeor classification, path-attenuation correction, radar meteorology, radar polarimetry.

## I. INTRODUCTION

DUAL-POLARIZED weather coherent radar systems can offer the opportunity to detect and identify different classes of hydrometeors in liquid, mixed, and ice phases that are usually present in stratiform and convective storms [1]–[3]. This important and appealing capability depends on the fact that dual-polarized radar measurements, such as copolar reflectivity  $Z_{hh}$ , differential reflectivity  $Z_{dr}$ , and the specific differential phase  $K_{dp}$ , are highly sensitive to physical properties of hydrometeors, such as composition, size, shape, and orienta-

tion [4]–[7]. Hydrometeor classification may strongly support rain-cloud microphysics investigation, quantitative detection of hailstorms, and correct tuning of precipitation rate retrieval algorithms [8]. Last but not least, hydrometeor identification may also be useful for flight assistance and weather nowcasting.

Most scientific literature about hydrometeor classification has been so far devoted to classification techniques that are designed for S-band dual-polarized weather radars (e.g., [9]–[12]). Hydrometeor polarimetric signatures, as is known, may strongly depend on the frequency that is used by the weather radar system. Theoretical and experimental evidence has shown that the precipitation dual-polarized responses at the S-band can substantially differ from the C-band ones (e.g., [13] and [14]). From an electromagnetic point of view, hydrometeor signatures at C-band may be significantly affected by the Mie resonance effects [14], [15].

Only recently, some works that are related to the exploitation of C-band measurements for hydrometeor classification have been presented [16]–[21]. The interest of assessing C-band hydrometeor classification may also emerge from the consideration that most mid- to high-latitude weather radars operate and are planned at C-band (e.g., [22]). Generally speaking, C-band radar systems may offer some advantages such as higher sensitivity, reduced antenna size, and overall lower cost, with respect to an S-band system with similar characteristics. On the other hand, rainfall path attenuation cannot be disregarded when inverting radar measurements at the C-band frequencies and above [8], [23], [24]. Dual-polarized weather radars may offer the advantage of polarization diversity and differential phase shift measurements to correct for precipitation path-attenuation effects in a fairly effective way (e.g., [25] and [26]), even though large statistical fluctuations and residual ambiguities may affect the overall accuracy (OA) [14].

In this paper, a fuzzy-logic classification method for C-band polarimetric radar data is presented. Since the hydrometeor classes are *a priori* arbitrarily identified and the radar response is derived from a scattering model, the classification approach may be labeled as *supervised* and *model based*. The goal is not to devise a new fuzzy-logic algorithm but, using an established approach, to: 1) extend it from S-band to C-band radar data; 2) handle both power and phase measurements, giving some details of the algorithmic approach at C-band; 3) show the improvements that are obtained using a C-band-tuned algorithm with respect to an S-band-based approach, which are directly applied to C-band data; and 4) evaluate the impact of path-integrated attenuation (PIA) exploiting a two-radar network. The investigation of this issue can be of practical interest, considering the increasing installations of dense C-band radar

Manuscript received June 11, 2006; revised May 18, 2007. This work was supported in part by the Region Abruzzo, L'Aquila, Italy, and in part by the Italian Department of Civil Protection, Rome, Italy.

F. S. Marzano is with the Department of Electronic Engineering, University of Rome "La Sapienza," 00184 Rome, Italy, and also with the CETEMPS Center of Excellence, University of L'Aquila, 67040 L'Aquila, Italy (e-mail: marzano@die.uniroma1.it).

D. Scaranari was with the Department of Electronic Engineering, University of Rome "La Sapienza," 00184 Rome, Italy. He is now with Sofiter System Engineering, 00142 Rome, Italy (e-mail: danielecaranari@tele2.it).

G. Vulpiani was with the CETEMPS Center of Excellence, University of L'Aquila, 67040 L'Aquila, Italy. He is now with Meteo France, 78195 Trappes, France (e-mail: gianfranco.vulpiani@meteo.fr).

Color versions of one or more of the figures in this paper are available online at <http://ieeexplore.ieee.org>.

Digital Object Identifier 10.1109/TGRS.2007.903399

networks, particularly, in European countries, and the fact that most operational radars are nowadays still single-polarized systems (e.g., [22]).

This paper is organized as follows. The hydrometeor radar scattering model is introduced in Section II, underlining the theoretical issues and the hydrometeor physical and electromagnetic modeling. The Fuzzy-logic Radar Algorithm for Hydrometeor Classification at C-band (FRAHCC) is illustrated in Section III. The devised algorithm can use both a reduced set of polarimetric observables, i.e.,  $Z_{hh}$  and  $Z_{dr}$ , and an extended one including  $Z_{hh}$ ,  $Z_{dr}$ , and  $K_{dp}$ , as detailed in Appendix A. A test of classification accuracy on synthetic data is also carried out. In Section IV, the FRAHCC technique is applied to data coming from C-band Doppler dual-polarized radars in network configurations that are located in Gattatico (GAT) and S. Pietro Capofiume (SPC) within the Po Valley in northern Italy. The main purpose is to show qualitative accuracy improvements with respect to the use of a similar algorithm that is tuned for S-band dual-polarized data. In Section V, the two coordinated C-band thunderstorm observations are exploited to implement a PIA correction procedure based either on a composite radar field approach or, more rigorously, on a network-constrained algorithm for attenuation compensation, using a variety of approaches that are summarized in Appendix B. The conclusions and remarks in Section VI end this paper.

## II. HYDROMETEOR RADAR SCATTERING MODEL AT C-BAND

A classification scheme is called *supervised*, apart from the methodology that was used, if measurements are assigned to a class with the user having foreknowledge of the existence of the classes themselves [34]. This knowledge may be derived from the scientific literature, field measurements, and experts' experience. Generally speaking, in order to set up a supervised classification for our purposes, we should gather combined *in situ* data of each identified hydrometeor class (e.g., from airborne-installed probes) and corresponding weather radar measurements [11]. This empirical task is rather difficult to accomplish and, anyway, may not be exhaustive. An alternative approach is to resort to a radar scattering model that simulates, as accurate as possible, polarimetric radar signatures and their relation to hydrometeor types. This model-based approach may offer some advantages, such as its flexibility and frequency scaling properties, but, on the other hand, it suffers from the assumptions that were made within the model itself. In this paper and similarly to [6]–[12], we will adopt a model-based supervised classification approach (as opposed to an empirical unsupervised technique).

As previously mentioned, dual-polarized radar responses at C-band may be significantly affected by hydrometeor path attenuation. If  $Z_{hhm}$  and  $Z_{vvm}$  (in  $\text{mm}^6 \cdot \text{m}^{-3}$ ) are the *measured* copolar reflectivity factors for horizontally and vertically polarized waves, respectively, they can be related to the corresponding equivalent reflectivity factors  $Z_{hh}$  and  $Z_{vv}$  by (e.g., [8])

$$Z_{hhm,vvm}(r) = Z_{hh,vv}(r)e^{-2 \int_{r_0}^r \frac{A_{hh,vv}(r')}{4.343} dr'} \quad (1)$$

where  $r$  (in kilometers) is the range, with  $r_0$  being the raincell starting range, whereas  $A_{hh}$  and  $A_{vv}$  (in decibels per kilometer) are the copolar specific attenuations for horizontally and vertically polarized waves, respectively.

In the following text, we will first summarize the radar scattering model and then apply it to characterize hydrometeor signatures.

### A. Polarimetric Radar Observables

If  $D_e$  is the equivolume sphere-equivalent diameter and  $N(D_e)$  represents the particle size distribution (PSD) for a specific hydrometeor, the copolar reflectivity factors  $Z_{hh,vv}$  are defined as (e.g., [8])

$$Z_{hh,vv} = \frac{\lambda^4}{\pi^5 |K|^2} \int_0^\infty \sigma_{hh,vv}(D_e) N(D_e) dD_e = \frac{\lambda^4 \langle \sigma_{hh,vv} \rangle}{\pi^5 |K|^2} \quad (2)$$

where  $K$  is the dielectric complex factor. In (2),  $\sigma_{hh,vv}$  is the copolar backscattering cross section, whereas the angle brackets stand for ensemble averaging over  $N(D_e)$ . The differential reflectivity  $Z_{dr}$  and specific differential phase  $K_{dp}$  are given by

$$Z_{dr} = 10 \log_{10} \left( \frac{Z_{hh}}{Z_{vv}} \right) = 10 \log_{10} \left( \frac{\langle \sigma_{hh} \rangle}{\langle \sigma_{vv} \rangle} \right) \quad (3)$$

$$K_{dp} = 10^{-3} \frac{180}{\pi} \times \lambda \text{Re} \left\{ \int_0^\infty N(D_e) [f_{hh}(r, D_e) - f_{vv}(r, D_e)] dD_e \right\} \quad (4)$$

where  $f_{hh,vv}$  is the forward scattering amplitude at horizontal or vertical polarization. Note that, in (3) and (4),  $Z_{dr}$  and  $K_{dp}$  are expressed in decibels and in degrees per kilometers, respectively, whereas  $D_e$  and  $\lambda$  are expressed in millimeters. We limit our attention to these observables, with the analysis of copolar correlation coefficient  $\rho_{hv}$  and linear depolarization ratio  $L_{dr}$  being beyond our scope.

Once the particle shape, orientation, and dielectric composition, together with  $N(D_e)$ , are known, a numerical solution can be adopted to derive both  $\sigma_{hh,vv}$  and  $f_{hh,vv}$ . The T-Matrix method, which is also known as the extended boundary condition method, is an effective numerical solution of the scattering problem for nonspherical particles by means of the electromagnetic equivalence theorem [27]. The T-Matrix approach has been extensively adopted in this paper.

### B. Modeling Hydrometeor Radar Signatures at C-Band

A correct microphysical and dielectric modeling of hydrometeors is essential to obtain meaningful simulations of polarimetric radar measurements. Radar simulations are necessary to set up the supervised classification scheme: the number of hydrometeor classes and their physical features are *a priori* defined in order to retrieve hydrometeor polarimetric signatures, such that no clustering algorithm is required. Detailed information

about several hydrometeor types can be found in [7], and here, we basically follow their approach, resorting to standard meteorological glossary in case of multiple choices [36]. In this paper, only ten hydrometeor classes have been established and named as follows: LD (*large drops*), LR (*light rain*), MR (*medium rain*), HR (*heavy rain*), H/R (*hail/rain mixture*), H (*hail*), G/SH (*graupel/small hail*), DS (*dry snow*), WS (*wet snow*), and IC (*ice crystals*). This means that we do not attempt to discriminate between vertically and horizontally oriented ice crystals as in [11]. Hydrometeor models, together with environmental temperature information, have been included in the scattering model simulation. Temperature, and particularly the freezing level, is a fundamental variable in hydrometeor classification schemes: some classes can physically exist at certain temperatures whereas others cannot. In order to keep the electromagnetic model simple enough, we have assumed that all particle shapes may be approximated by spheroids [7]. This approximation, which is realistic for raindrops and mixed-phase drops, may fail for ice hydrometeors, which exhibit a large variety of shapes [36].

In the following paragraphs, the adopted microphysical and dielectric parameterization is briefly discussed; details are shown in Table I for each hydrometeor class. It should be kept in mind that the adopted spheroidal shape may be unrealistic when representing IC and DS hydrometeors, whereas the modeling of mixed-phase classes, such as H/R and WS, is still an open issue. These limitations reflect, of course, in the OA of the model-based FRAHCC scheme.

*PSD*: A normalized Gamma function of the form

$$N(D_e) = N_w f(\mu) \left( \frac{D_e}{D_0} \right)^\mu e^{-(3.67+\mu)\frac{D_e}{D_0}} \quad (5)$$

has been assumed to represent the raindrop size distribution (e.g., [8]). In (5),  $f(\mu)$  is a function of the shape parameter  $\mu$  only,  $D_0$  (in millimeters) is the median volume drop diameter, and  $N_w$  (per millimeter per cubic meter) is the intercept parameter that is proportional to  $W/(\rho_w D_0^4)$ , with  $W$  being the liquid water content and  $\rho_w$  being its density. Regarding the other hydrometeor particles, a classical inverse-exponential PSD of the form  $N_0 \exp(-\Lambda D_e)$  has been assumed (see Table I). Note that, in case of inverse-exponential distributions, the  $\Lambda$  parameter is often expressed in terms of precipitation rate as in the case of DS and WS following the Sekhon–Srivastava PSD [7]. In these cases, we have converted the expected precipitation rate variability into equivalent  $\Lambda$  variability.

*Axis Ratio*: As previously mentioned, the shape of all hydrometeors has been represented by a spheroid, with the orientation and axis ratio  $r_a(D_e)$  (i.e., the ratio between the particle minor and major axes) depending on the hydrometeor category. Here, we have assumed that  $r_a$  follows the Beard and Chuang model [30] (hereinafter, BC) for rain. Small hail (for  $D < 10$  mm) is treated as spherical particle, whereas, for larger hail,  $r_a$  is uniformly distributed between 1 and 1.67 for H. The G/SH axis ratio is assumed to be linearly varying between 1 (sphere) and 1.7. Regarding the DS, WS, and IC classes,  $r_a$  is supposed to be linearly varying in the ranges [1.0, 1.2],

[1.0, 1.8], and [1.0, 2.0], respectively, with the addition of a uniformly distributed random number between 0 and 0.1.

*Hydrometeor Orientation*: For raindrops, DS, and WS, the symmetry axis is considered to be tilted, with respect to the reference system, by an angle ( $\beta$ ) following a zero-mean Gaussian distribution with  $5^\circ$  of standard deviation. The tilt angle of  $H$  is randomly distributed with a mean fixed to a  $90^\circ$  and a standard deviation of  $5^\circ$  for half simulations and varies between  $0^\circ$  and  $90^\circ$  with a standard deviation of  $5^\circ$  for the remaining half set. The latter configuration should reproduce the tumbling feature of hail [7]. For G/SH,  $\beta$  is uniformly distributed between  $0^\circ$  and  $180^\circ$  (i.e., no preferential state). Regarding the IC class,  $\beta$  is randomly distributed with a mean value of  $0^\circ$  and  $90^\circ$  for horizontally and vertically oriented crystals, respectively, with the standard deviation being of  $5^\circ$ .

*Dielectric Composition*: The water and ice relative dielectric constants  $\epsilon_r$  are derived from the Ray [28] and Warren [31] models, respectively (hereinafter, RM and WM). The G/SH class has been modeled with a linear-mixing dielectric constant (hereinafter, LM) of water and ice, with inclusions of water randomly varying between 20% and 45%. For DS, a second-order Maxwell–Garnet mixing dielectric formula (hereinafter, SOMG) between air and ice has been assumed [8], with the fraction of air inclusions linearly increasing with snow diameter. The WS class has been modeled with a linear-mixing dielectric constant between water and ice, with the water inclusions varying between 1% and 10%.

A set of 2000 scattering simulations for each hydrometeor class has been carried out in order to have a statistically significant, but relatively small, data set of simulated polarimetric signatures. Examples at the C-band are shown in Fig. 1, where the simulated results are plotted on the two observable planes ( $Z_{hh} - Z_{dr}$ ) and ( $Z_{hh} - K_{dp}$ ). The figure shows a relatively high degree of ambiguity in hydrometeor radar signatures within this modeling framework. Graupel (G/SH), medium rain (MR), and wet snow (WS)  $Z_{hh}$  responses are largely overlapped; ice crystal signature is mixed with light rain, medium rain, and dry snow. Hail and hail/rain can generate  $Z_{dr}$  around 0 dB, and for  $Z_{hh} > 50$  dBZ, the  $Z_{dr}$  of graupel tends to mix with them.

With respect to S-band measurements, C-band signatures are more sensitive to the particle shape for hydrometeor sizes between 4 and 8 mm and, in general, present larger values of  $Z_{dr}$  and  $K_{dp}$  and lower values of the copolar correlation [13], [14]. The most relevant differences between the two band behaviors have been found for the LD, MR, HR, and H/R classes. Specifically, it is worth noting that: 1) the  $Z_{dr}$  at the S-band is not usually larger than 3.5 dB, while, at the C-band, LD and HR may give rise to a  $Z_{dr}$  that is even larger than 5 dB and 2) the  $Z_{hh}$  values for LD and H/R may be higher of several decibels. The retrieval of  $K_{dp}$  is also affected by the backscattering differential phase shift  $\delta_{hv}$ , which is no more negligible at C-band [8], [23]. The key advantage of  $K_{dp}$  at C-band is the capability to discriminate between rain and ice hydrometeors (see Fig. 1). The copolar correlation coefficient  $\rho_{hv}$  has been simulated as well. Its values at C-band are between 0.9 and 1: as the inhomogeneity and asymmetry of hydrometeors increase, it tends to assume lower values [13], [14]. Thus, LR and MR have a  $\rho_{hv}$  of about 1, while LD, H/R,

TABLE I  
MICROPHYSICAL AND DIELECTRIC MODELS ADOPTED TO SIMULATE HYDROMETEOR POLARIMETRIC RADAR SIGNATURES (RM: RAY'S MODEL, WM: WARREN'S MODEL, LM: LINEAR MIXING, SOMG: SECOND-ORDER MAXWELL GARNET, BC: BEARD–CHUANG). RAND ( $x$ ) MEANS A UNIFORM RANDOM NOISE OF WIDTH  $x$

Hydrometeor class	Particle size distribution parameters	Relative dielectric constant ( $\epsilon_r$ ) model	Axis ratio ( $r_a$ ) model
	$D_e$ [mm] Gamma PSD: $D_0$ [mm], $N_w$ [ $\text{mm}^{-1} \text{m}^{-3}$ ], $\mu$ Exponential PSD: $N_0$ [ $\text{mm}^{-1} \text{m}^{-3}$ ], $\Lambda$ [ $\text{mm}^{-1}$ ]	Temperature T [°C]	Tilt angle ( $\beta$ ) Gaussian model
Large Drops (LD)	$0.6 \leq D_e \leq 7.0$ $1.3 \leq D_0 \leq 3.6, 15.0 \leq N_w \leq 150.0$ $-0.94 < \mu \leq 0.87$	RM	BC
		$-5.0 \leq T \leq 35.0$	$\bar{\beta} = 0^\circ, \sigma_\beta = 5^\circ$
Light Rain (LR)	$0.6 \leq D_e \leq 7.0$ $0.5 \leq D_0 \leq 1.4, 10^3 \leq N_w \leq 2.1 \cdot 10^4$ $-1.0 < \mu \leq 4.0$	RM	BC
		$0 \leq T \leq 40.0$	$\bar{\beta} = 0^\circ, \sigma_\beta = 5^\circ$
Medium Rain (MR)	$0.6 \leq D_e \leq 7.0$ $1.4 \leq D_0 \leq 2.0, 10^3 \leq N_w \leq 10^4$ $-1.0 < \mu \leq 4.0$	RM	BC
		$0 \leq T \leq 40.0$	$\bar{\beta} = 0^\circ, \sigma_\beta = 5^\circ$
Heavy Rain (HR)	$0.6 \leq D_e \leq 7.0$ (8.0 with Hail) $1.8 \leq D_0 \leq 3.2, 2 \cdot 10^3 \leq N_w \leq 9 \cdot 10^3$ $-1.0 < \mu \leq 4.0$	RM	BC
		$0 \leq T \leq 40.0$	$\bar{\beta} = 0^\circ, \sigma_\beta = 5^\circ$
Hail (H)	$5.0 \leq D_e \leq 30.0$ $0.4 \leq \Lambda \leq 1.0$ $100.0 \leq N_0 \leq 300.0$	WM	$1.0 \leq r_a \leq 1.1$ if $D_e \leq 10$ mm
		$-20.0 \leq T \leq 20.0$	$1.0 \leq r_a \leq 1.67$ if $D_e > 10$ mm $0^\circ \leq \bar{\beta} \leq 90^\circ, \sigma_\beta = 5^\circ$
Hail/Rain (H/R)	As for the H and HR classes	As for the H and HR classes	As for the H and HR classes
Graupel/Small Hail (G/SH)	$1.0 \leq D_e \leq 5.0$ $0.5 \leq \Lambda \leq 1.6$ $10.0 \leq N_0 \leq 270.0$	LM	$1.0 \leq r_a \leq 1.7 + \text{rand}(0.1)$
		$-50.0 \leq T \leq 10.0$	$0^\circ \leq \bar{\beta} \leq 90^\circ, \sigma_\beta = 5^\circ$
Dry Snow (DS)	$1.0 \leq D_e \leq 15.0$ $2.2 \leq \Lambda \leq 8.8$ $2380 \leq N_0 \leq 42000$	SOMG	$1.0 \leq r_a \leq 1.2 + \text{rand}(0.1)$
		$-51.0 \leq T \leq 0.0$	$\bar{\beta} = 0^\circ, \sigma_\beta = 5^\circ$
Wet Snow (WS)	$1.0 \leq D_e \leq 15.0$ $1.8 \leq \Lambda \leq 3.1$ $1515 \leq N_0 \leq 4800$	LM	$1.0 \leq r_a \leq 1.8 + \text{rand}(0.1)$
		$-2.5 \leq T \leq 2.5$	$\bar{\beta} = 0^\circ, \sigma_\beta = 5^\circ$
Ice Crystals (IC)	$0.2 \leq D_e \leq 4.8$ $1.1 \leq \Lambda \leq 3.0$ $1.0 \leq N_0 \leq 41.0$	WM	$1.0 \leq r_a \leq 2.0 + \text{rand}(0.1)$
		$-72.5 \leq T \leq -5.5$	$0^\circ \leq \bar{\beta} \leq 90^\circ, \sigma_\beta = 5^\circ$

and G/SH are characterized by decreasing values down to 0.9 for bigger and more asymmetric particles.

### III. FUZZY CLASSIFICATION METHOD FOR C-BAND DATA

As previously noted, at C-band, path attenuation is relevant and cannot be always neglected. Furthermore, data that are provided by radar measurements or T-Matrix numerical simulations tend to overlap significantly, as shown by Fig. 1. All these aspects make fuzzy-logic one of the best solutions for the hydrometeor classification problem [9]–[11]. Fuzzy-logic techniques are fairly simple and flexible to set up, and their behavior tends to be robust to noisy data [8]. A fuzzy-logic classification scheme, which is supervised by the

C-band scattering model that was discussed in Section II, will be illustrated in the next two sections.

#### A. Fuzzy-Logic Radar Algorithm at C-Band

A fuzzy-logic system basically provides a nonlinear mapping of input data vectors into scalar outputs [33]. Any fuzzy-logic algorithm consists of three main stages: 1) fuzzification; 2) inference; and 3) defuzzification (e.g., [11]).

In this paper, we have considered, as input data vector, the combination of reflectivity  $Z_{\text{hh}}$ , differential reflectivity  $Z_{\text{dr}}$ , and environmental temperature  $T$ . This choice is mainly dictated by the radar system specifications that were used for algorithm testing (see Section IV). In order to generalize the C-band methodology to polarimetric radars, we have also

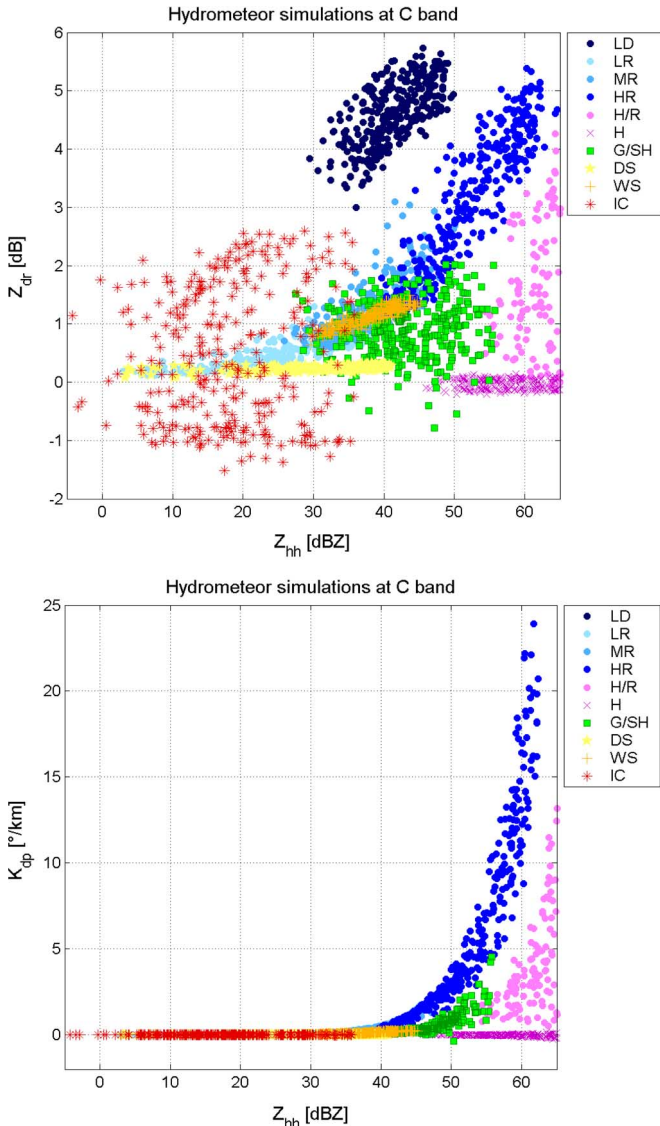


Fig. 1. Polarimetric radar simulations of (top panel) copolar horizontally polarized reflectivity  $Z_{hh}$  and differential reflectivity  $Z_{dr}$ , and (bottom panel)  $Z_{hh}$  and differential phase shift  $K_{dp}$  for ten hydrometeor classes at C-band. See text for details.

considered the possible use of the specific differential phase  $K_{dp}$ , but we have not included  $\rho_{hv}$  and  $L_{dr}$  into our analysis.

In the FRAHCC technique with a reduced set of inputs, the fuzzification stage is characterized by ten bidimensional membership functions (MBFs) for  $Z_{hh}$  and  $Z_{dr}$ , and ten monodimensional MBFs for temperature. The temperature for each radar bin is evaluated by means of a vertical radio-sounding profile that is realized in the proximity of the storm. In the absence of this kind of measurement, a standard temperature gradient can be assumed as a first approximation. The outputs of the MBFs are called membership degrees, and they can assume values ranging from 0 (no membership) to 1 (maximum membership). The definition of MBFs is a fundamental task that affects the classification accuracy. The starting point has been a set of MBFs, which is originally described in [7] and implemented as a general fuzzy-logic scheme by Zrnic *et al.* [10]. This scheme was designed for S-band data, so that it cannot be applied in a straightforward way to C-band

radar data [19], [21]. As seen, resonance effects due to Mie scattering cannot be neglected at C-band, and MBFs must be suitably modified. The MBFs that were adopted in this paper have trapezoidal forms whose analytical expressions have been derived through an accurate analysis of simulations, which were carried out for C-band using a T-Matrix solution technique. The linear fuzzy thicknesses can be different for each hydrometeor class. Temperature MBFs are also trapezoidal functions, which are derived from Zrnic *et al.* [10] and further adapted in [19] and [21]. For each hydrometeor class, analytical expressions of the bidimensional MBFs, which are related to C-band observable couples  $(Z_{hh}, Z_{dr})$  and  $(Z_{hh}, K_{dp})$  and to environmental temperature  $T$ , are explicitly reported in Appendix A.

The inference rule  $I_{Ri}$  for the  $i$ th class is based on the product of membership degrees that were derived from MBFs as it follows when only  $Z_{hh}$  and  $Z_{dr}$  are available, i.e.,

$$I_{Ri} = M_{Zi}(Z_{hh}, Z_{dr})M_{Ti}(T) \tag{6}$$

where  $i = 0 - 9$ , and the  $M_{Zi}$  and  $M_{Ti}$  are the MBFs for the  $(Z_{hh}, Z_{dr})$  and  $T$  of the  $i$ th class, as defined in Appendix A. The choice of the product in (6), instead of linear combination, has the purpose to limit classification errors as far as possible: if, for a given class, one measurement is significantly out of range, the low value of the corresponding MBF will definitely suppress the class. When  $K_{dp}$  estimates from  $\Phi_{dp}$  measurements are also available, a hybrid inference rule can be designed as follows:

$$I_{Ri} = [w_{Zi}M_{Zi}(Z_{hh}, Z_{dr}) + w_{Ki}M_{Ki}(Z_{hh}, K_{dp})] M_{Ti}(T) \tag{7}$$

where  $M_{Zi}$  and  $M_{Ki}$  are MBFs for  $(Z_{hh}, Z_{dr})$  and  $(Z_{hh}, K_{dp})$ , respectively, with  $w_{Zi}$  and  $w_{Ki}$  being the arbitrary weights for the  $i$ th class. From the numerical analysis that is discussed in the next paragraph, the optimal weights have been set to  $w_{Zi} = 1$  and  $w_{Ki} = 0.8$ , except for G/SH, where  $w_{Zi} = 0.8$  and  $w_{Ki} = 0.1$ . Indeed, (6) can be seen as a particular case of (7), where  $w_{Zi} = 1$  and  $w_{Ki} = 0$ .

The defuzzification is carried out by a maximum-value rule that is applied to either (6) or (7), giving the estimated hydrometeor class index  $i_c$  to which the radar bin is assigned, i.e.,

$$\hat{i}_c = \text{Max}_i[I_{Ri}], \quad i = 0, 1, \dots, 9 \tag{8}$$

where  $\text{Max}_i$  is the maximum operator with respect to the  $i$ th class. If two or more rules present the same maximum value, the NC (*nonclassified*) label is assigned to the radar bin.

### B. Tests on Synthetic Radar Data

In order to evaluate the expected classification accuracy, we have generated a training and test data set that consists of 1000 independent simulations of  $Z_{hh}$ ,  $Z_{dr}$ , and  $K_{dp}$  for each hydrometeor class, with the environmental temperature  $T$  uniformly distributed inside specific intervals. With the aim of reproducing the measurement process at C-band, a zero-mean Gaussian noise with standard deviations equal to 1 dBZ, 0.3 dB, and  $0.2^\circ/\text{km}$  has been added to  $Z_{hh}$ ,  $Z_{dr}$ , and  $K_{dp}$ , respectively.

TABLE II  
CONTINGENCY TABLE OBTAINED USING C-BAND FUZZY-LOGIC CLASSIFICATION ALGORITHM  
(FRAHCC) APPLIED TO C-BAND  $Z_{hh}$  AND  $Z_{dr}$  SIMULATED NOISY DATA

2 radar obs		SIMULATION										C-band UA
		LD	LR	MR	HR	H/R	H	G/SH	DS	WS	IC	
CLASSIFICATION	LD	98%	2%	2%	2%	0%	0%	0%	0%	0%	0%	94%
	LR	0%	73%	9%	0%	0%	0%	2%	1%	3%	0%	83%
	MR	0%	15%	66%	8%	0%	0%	4%	0%	8%	0%	65%
	HR	0%	0%	18%	81%	2%	0%	1%	0%	0%	0%	79%
	H/R	0%	0%	0%	1%	79%	13%	2%	0%	0%	0%	83%
	H	0%	0%	0%	0%	11%	65%	2%	0%	0%	0%	84%
	G/SH	0%	2%	2%	0%	0%	6%	63%	46%	4%	1%	51%
	DS	0%	0%	0%	0%	0%	0%	1%	22%	0%	8%	70%
	WS	0%	0%	0%	0%	0%	0%	2%	1%	46%	0%	94%
	IC	0%	0%	0%	0%	0%	0%	5%	14%	0%	85%	81%
	PA	98%	73%	66%	81%	79%	65%	63%	22%	46%	85%	OA=68%
	NC	2%	7%	4%	8%	9%	16%	17%	16%	38%	6%	NC <sub>av</sub> =12%

Contingency tables, which are also known as confusion matrices, are used to evaluate classification accuracy on either real or synthetic data [34]. If true inputs are on the columns and classified outputs are along the rows, the diagonal elements give a measure of the correct classifications, while extra diagonal elements indicate the exclusion errors along the matrix columns and the inclusion errors along the matrix rows. The percentage of correctly classified samples with respect to the total of each class is called producer accuracy (PA), while the same percentage with respect to the sum along each row is called user accuracy (UA). UA is a measure of the inclusion errors and expresses the probability that a sample, which is classified in a given class, really belongs to that class; its average is here called  $UA_{av}$ . The percentage ratio between the correctly classified samples over the total is called OA. The complement to 100% of the sum along each column provides the percentage of nonclassified (NC) samples, while its average ( $NC_{av}$ ) on the ten classes is an effective indicator of robustness to noise.

The contingency table, which is obtained using the FRAHCC scheme, is reported in Table II. As expected from Fig. 1, LD, LR, H/R, and H present high UA, with their signature being quite distinct. In terms of UA results, worse performances are noted for G/SH and MR, whereas the DS, WS, and IC classes are in the middle. Because of radar signature overlapping in the polarimetric observable planes (see Fig. 1), the PA and NC for the WS class are not as good as those for the other classes. For comparison, classification results using S-band MBFs that are applied to C-band data are reported in Table III. This procedure is not physically correct, but it can be applied for operational purposes (e.g., [16], [19], and [37]). From Tables II and III, the improvements of the hydrometeor classification accuracy, due to the proper use of C-band MBFs, are quite evident: OA goes from 53% to 68%, whereas  $NC_{av}$  goes from 24% to 12%.

Better results can be obtained using  $K_{dp}$  estimates from differential phase shift  $\Phi_{dp}$  measurements, if available. Indeed, differential phase data should be carefully used at C-band due to possible contribution of  $\delta_{hv}$ , even negative values of  $K_{dp}$  (related to resonance effects), nonuniform beam filling, and

large statistical fluctuations that are caused by lower  $\rho_{hv}$  [12], [13]. With this additional observable, a fuzzifier with hybrid inference rules can be designed by adopting a multiplicative or an additive inference rule to combine the MBFs  $M_{Zi}$  and  $M_{Ki}$ .

A systematic comparison, in terms of relative contingency tables, has shown that the additive rule, as in (7), with  $w_{Zi} = 1$  and  $w_{Ki} = 0.8$  for all classes, gives  $OA = 73\%$ ,  $UA_{av} = 78\%$ , and  $NC_{av} = 4\%$  versus  $OA = 68\%$ ,  $UA_{av} = 78\%$ , and  $NC_{av} = 12\%$  that are obtainable by adopting a multiplicative inference rule. A further sensitivity test has prompted the change of the weights  $w_Z = 0.8$  and  $w_K = 0.1$  only for G/SH, getting the optimal results of  $OA = 75\%$ ,  $UA_{av} = 79\%$ , and  $NC_{av} = 3\%$ , as given in Table IV. Looking at the UA outputs, the most noticeable improvements are for the H/R, H, and G/SH classes. An improvement in the snow class discrimination may be obtained if further polarimetric observables are used [6].

We might wonder how much C-band PIA may affect hydrometeor classification accuracy. In other words, it is worth investigating the impact of using noisy  $Z_{hhm}$ , instead of noisy  $Z_{hh}$ , on FRAHCC performance [see (1)]. This evaluation is quite difficult to assess as it depends on the specific hydrometeor range profile, which is highly variable. Moreover, even if path attenuation may be corrected using proper techniques (e.g., [25]), a residual error due to these algorithms should also be taken into account, mainly as an overall underestimation [26]. Nevertheless, we have performed a numerical experiment assuming a schematic scenario. The basic idea is to suppose that each random simulation, which was previously analyzed, is hypothetically measured after path attenuation due to either a rain or graupel slab. The noisy simulated values of  $Z_{hh}$  have been varied by an increasing negative bias, due to PIA, between  $-0.5$  and  $-5$  dB. This means that, if, at C-band, maximum  $A_{hh}$  is about 0.5 dB/km for rain and 0.4 dB/km graupel, the shortest one-way path can be on the order of 5 and 6 km for rain and graupel, respectively. In order to be physically consistent, the differential propagation attenuation  $A_{dp} = A_{hh} - A_{vv}$  has been approximately set, for each simulation, to be equal to  $0.3 A_{hh}$  and  $0.18 A_{hh}$  for rain and graupel slabs, respectively.

TABLE III  
CONTINGENCY TABLE OBTAINED USING S-BAND FUZZY CLASSIFICATION MBFS [16] APPLIED TO C-BAND  $Z_{hh}$  AND  $Z_{dr}$  SIMULATED NOISY DATA

2 radar obs		SIMULATION										S-band
		LD	LR	MR	HR	H/R	H	G/SH	DS	WS	IC	UA
CLASSIFICATION	LD	91%	6%	17%	11%	0%	0%	1%	0%	1%	0%	71%
	LR	0%	70%	7%	0%	0%	0%	2%	1%	3%	0%	85%
	MR	0%	15%	56%	6%	0%	0%	4%	0%	7%	0%	63%
	HR	0%	0%	13%	24%	5%	0%	2%	0%	0%	0%	53%
	H/R	0%	0%	0%	0%	58%	20%	2%	0%	0%	0%	72%
	H	0%	0%	0%	0%	10%	46%	1%	0%	0%	0%	80%
	G/SH	0%	2%	1%	0%	0%	9%	63%	49%	4%	1%	49%
	DS	0%	0%	0%	0%	0%	0%	1%	20%	0%	8%	69%
	WS	0%	0%	0%	0%	0%	0%	2%	1%	46%	0%	94%
	IC	0%	0%	0%	0%	0%	0%	5%	13%	0%	52%	73%
PA	91%	70%	56%	24%	58%	46%	63%	20%	46%	52%	OA=53%	
NC	9%	7%	5%	58%	26%	26%	17%	15%	38%	39%	NC <sub>av</sub> =24%	

TABLE IV  
SAME AS IN TABLE II BUT APPLIED TO C-BAND  $Z_{hh}$ ,  $Z_{dr}$ , AND  $K_{dp}$  SIMULATED NOISY DATA

3 radar obs		SIMULATION										C-band
		LD	LR	MR	HR	H/R	H	G/SH	DS	WS	IC	UA
CLASSIFICATION	LD	98%	3%	2%	0%	0%	0%	3%	0%	0%	0%	92%
	LR	0%	76%	9%	0%	0%	0%	2%	1%	7%	0%	80%
	MR	0%	16%	66%	8%	0%	0%	4%	0%	19%	0%	58%
	HR	0%	0%	21%	87%	0%	0%	2%	0%	1%	0%	78%
	H/R	1%	0%	0%	0%	90%	10%	3%	0%	0%	0%	86%
	H	0%	0%	0%	0%	8%	77%	1%	0%	0%	0%	90%
	G/SH	0%	1%	0%	0%	0%	5%	66%	35%	1%	1%	60%
	DS	0%	0%	0%	0%	0%	0%	7%	45%	1%	9%	72%
	WS	0%	0%	1%	0%	0%	0%	4%	1%	63%	0%	91%
	IC	0%	0%	0%	0%	0%	0%	5%	16%	0%	87%	81%
PA	98%	76%	66%	87%	90%	77%	66%	45%	63%	82%	OA=75%	
NC	0%	4%	1%	4%	2%	8%	3%	1%	8%	1%	NC <sub>av</sub> =3%	

TABLE V  
CLASSIFICATION RESULTS IN TERMS OF AVERAGE USER ACCURACY  $UA_{av}$ , OA, AND AVERAGE NONCLASSIFIED AVERAGE  $NC_{av}$  WHEN ADDING A NEGATIVE BIAS TO TWO ( $Z_{hh}$  AND  $Z_{dr}$ ) OR THREE ( $Z_{hh}$ ,  $Z_{dr}$ , AND  $K_{dp}$ ) OBSERVABLE DATA USING FRAHCC

	Bias $Z_{hh}$ (dBZ)	Bias $Z_{dr}$ (dB)	2 radar observables			3 radar observables		
			$UA_{av}$ (%)	OA (%)	$NC_{av}$ (%)	$UA_{av}$ (%)	OA (%)	$NC_{av}$ (%)
Rain slab	-0.5	-0.15	79	69	12	80	76	3
	-1.5	-0.45	77	67	12	77	74	4
	-2.5	-0.75	72	59	16	71	67	6
	-3.5	-1.05	65	50	21	65	58	9
	-4.5	-1.35	56	43	28	60	51	14
Graupel slab	-0.5	-0.09	79	69	12	80	76	3
	-1.5	-0.27	79	68	12	79	76	3
	-2.5	-0.45	77	66	13	76	73	4
	-3.5	-0.63	73	61	14	72	67	5
	-4.5	-0.81	69	56	16	68	61	7

Table V shows the impact of simulated rain and graupel PIA in terms of  $UA_{av}$ , OA, and  $NC_{av}$ . These numbers should be compared with those of Tables II–IV. As expected, as PIA increases, the OA decreases, remaining larger

than about 41% with two polarimetric observables and about 49% with three polarimetric observables. The overall degradation of the classification due to PIA errors may be larger than 25%.

#### IV. HYDROMETEOR CLASSIFICATION AT C-BAND

Available radar data refer to a convective episode that occurred in the region between two dual-polarized C-band systems: 1) the SPC and 2) GAT radars. They are both located in the Po valley, about 90 km far apart, and are managed in a network model by the Emilia-Romagna Hydro-Meteorological Service (ARPA-SIM) to produce regional composite products for civil protection warning [19], [21], [35].

##### A. C-Band Radar System Specifications

The dual-polarization GPM-500C radars are placed on towers and equipped with Cassegrain parabolic antennas (without radome cover), providing a half-power beamwidth of  $1.0^\circ$  and a directivity of about 45 dB [35]. The klystron peak power is 250 kW at 5.6 GHz with an alternating horizontal-vertical polarization transmission and dual pulse repetition frequency system for velocity dealiasing. Pulse widths can be  $0.5 \mu\text{s}$  (i.e., short pulse with a resampled bin resolution of 250 m using time decimation) and  $1.5 \mu\text{s}$  (i.e., long pulse with a resampled bin resolution of 1500 m using time decimation). The receiver sensitivity is equal to  $-113 \text{ dBm}$ . The typically used maximum ranges are 250 km (with long pulse) and 125 km (with short pulse), for the intensity and velocity mode, respectively. Self-contained software is used to remotely operate and archive radar data of measured  $Z_{\text{hhm}}$  and  $Z_{\text{drm}}$ .

Radar data are acquired with a prescribed scanning strategy during operational activity, consisting of 15 elevations with an average angular spacing of  $1^\circ$ . The radial spatial resolution is set to 250 m for short ranges (i.e., 125 km) and to 1500 m for long-range (i.e., 250 km) scans, with the latter one being carried out only twice per hour. Time sampling of radar volume data is such that there are four acquisitions per hour (i.e., every 15 min), even though the dual-polarized mode is performed every half an hour. Procedures to correct for gas absorption, to remove ground-clutter echoes, and to identify anomalous propagation conditions are routinely applied [35].

##### B. Case Study

During the night between May 19, 2003, and May 20, 2003, a cold front, arriving from northwest and moving across the Alps, caused a deep convective event in the flat lands of northeast Italy within the area that is covered by the two radars GAT and SPC. An intense hailstorm developed for some hours within this region. The storm core, which was characterized by high values of reflectivity (50–60 dBZ), was in the range of about 55–60 km from SPC and 30–35 km from GAT. Examples of reflectivity and differential reflectivity vertical sections, along the two-radar connection line, are illustrated in Figs. 2 and 3. Radar sections refer to data acquired on May 20, 2003, at 16:34 GMT.

These figures display the range height indicators (RHIs) of the measured reflectivity  $Z_{\text{hhm}}$  and the differential reflectivity  $Z_{\text{drm}}$  for GAT and SPC radars, respectively, along the reference line, namely, the line connecting the positions of the two radars.

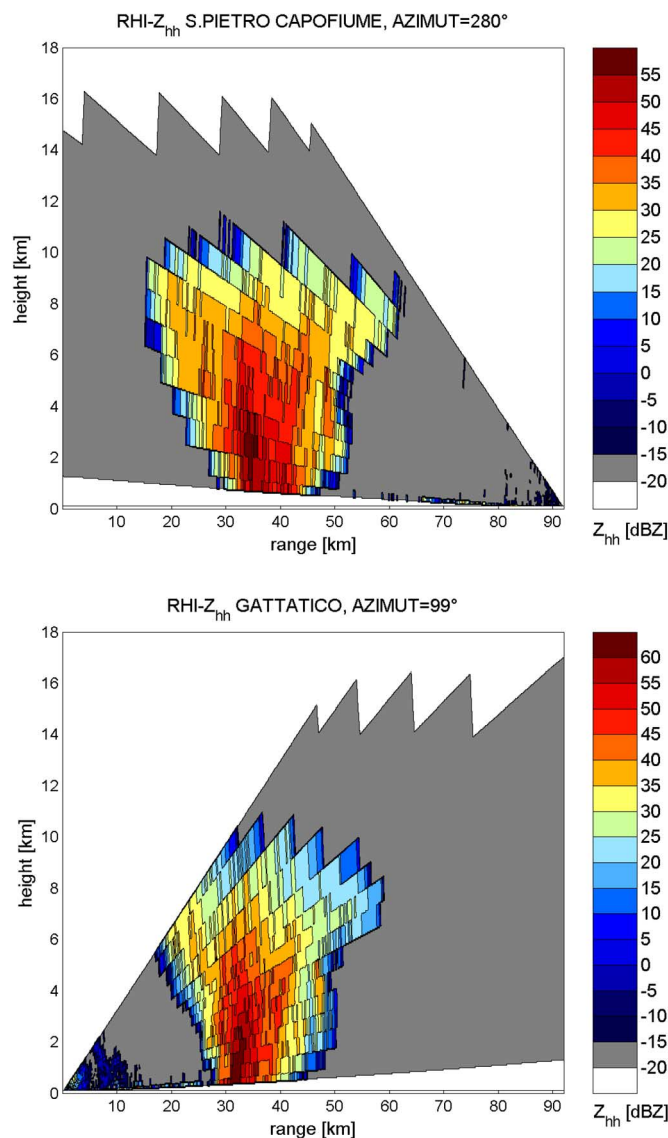


Fig. 2. Vertical section (RHI) of measured copolar horizontally polarized reflectivity  $Z_{\text{hhm}}$  with respect to the line-of-sight between the two C-band radar systems in Italy on May 20, 2003, at 16:34 GMT. The SPC radar is on the top panel, whereas the GAT radar is on the bottom panel.

From the  $Z_{\text{drm}}$  sections, it is possible to note the different attenuation zones in the two regions behind the convective core, depending on the different points of view of the two radars. The attenuation signature is clearly highlighted by analyzing the first elevation rays of  $Z_{\text{hhm}}$  and  $Z_{\text{drm}}$  of each radar along the reference line connecting them.

##### C. Hydrometeor Classification Results

Reflectivity and differential reflectivity data that are available from the two radars GAT and SPC have been first classified with the previously described FRAHCC technique, disregarding path-attenuation effects (i.e., assuming  $Z_{\text{hhm}} \cong Z_{\text{hh}}$  and  $Z_{\text{drm}} \cong Z_{\text{dr}}$ ). The temperature vertical average profile has been retrieved from a vertical radio sounding that was made at the SPC meteorological station.

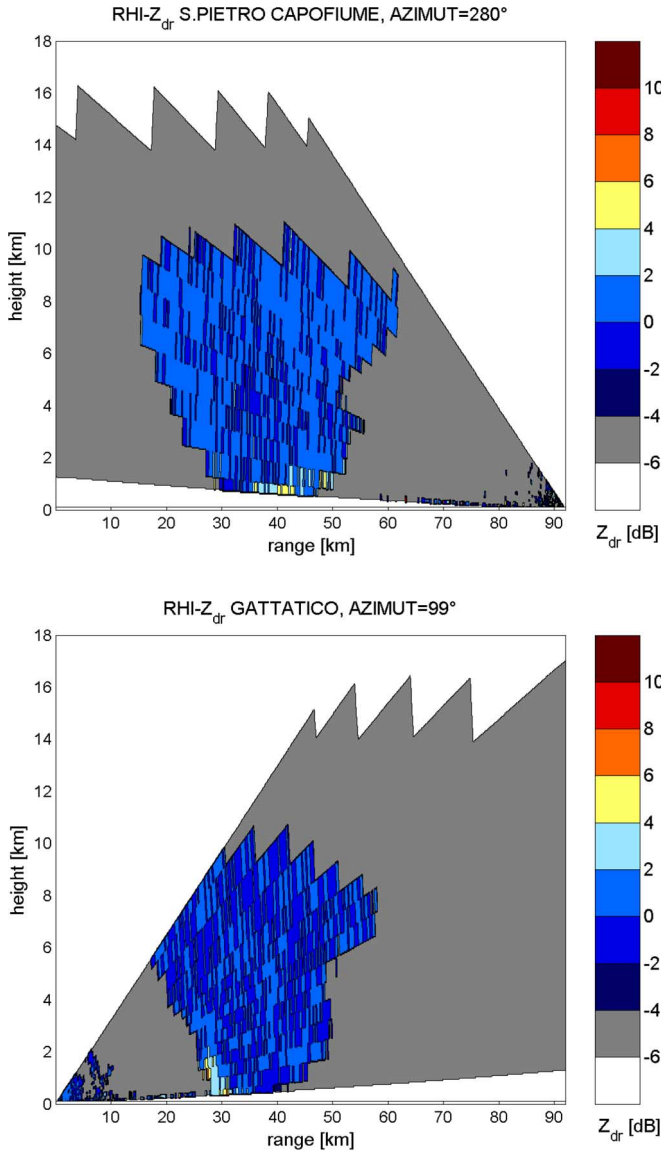


Fig. 3. Same as in Fig. 2 but for the measured differential reflectivity  $Z_{dr,m}$ .

Since truth data regarding the storm on the connection line are unavailable, only qualitative tests can be carried out. This visual inspection is aimed at evaluating the microphysical consistency of the hydrometeor field and the information content of each algorithmic choice [10]. As an example, the hydrometeor classification results that were obtained by using the FRAHCC technique are shown in Fig. 4 for the SPC radar. For comparison, corresponding results that were obtained by using MBFs that are valid at the S-band (applied to C-band data) are illustrated in Fig. 5.

Accuracy improvements can be recognized by direct observations of the RHI diagrams, first with the S-band MBFs and then with the C-band MBFs. The number of nonclassified (NC) radar bins considerably decreases, particularly, for GAT radar measurements, and ice crystal detection (IC) is now performed in a more realistic way. Classification results are also physically self-consistent: the hail core (H and H/R) is correctly detected at the center of the convective storm, graupel (G/SH) is reasonably identified all around the hail core, rain is present only at low

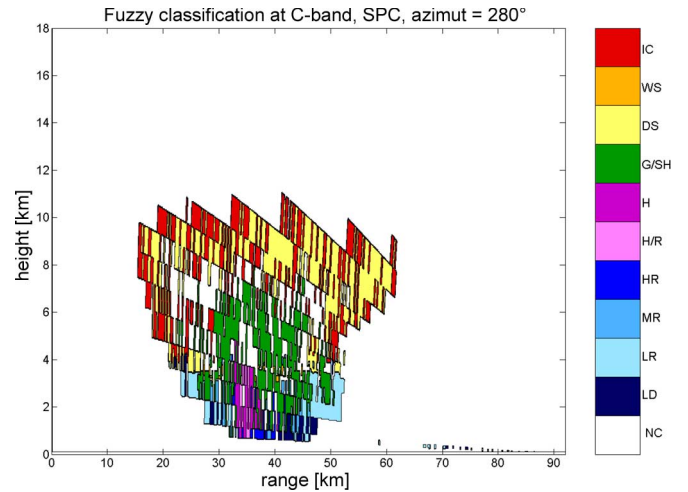


Fig. 4. Fuzzy-logic hydrometeor classification, using the FRAHCC technique that was given in (6) and (8), that is applied to the C-band radar data displayed in Figs. 2 and 3, along the line-of-sight between the two radar systems, as seen from the SPC radar.

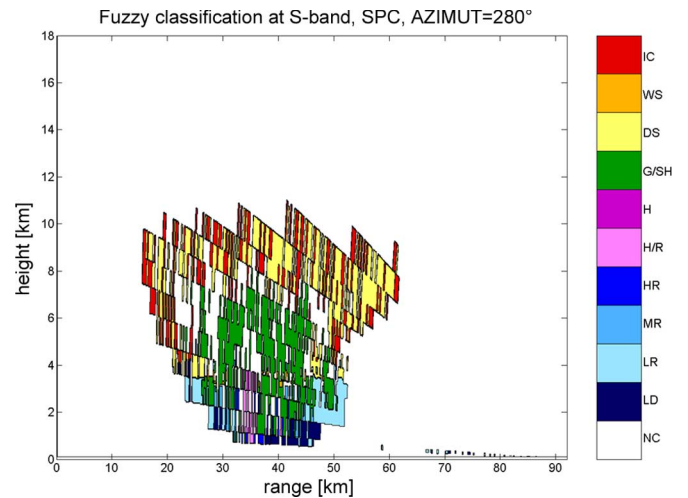


Fig. 5. Same as in Fig. 4, but using MBFs developed for S-band.

altitude (different shades of blue), while snow and ice crystals (DS, WS, and IC) are properly found within the top layers of the storm.

### V. IMPACT OF PATH ATTENUATION AT C-BAND

As earlier proven, an improvement of classification accuracy can be obtained by using  $K_{dp}$  estimates from fully polarimetric radar measurements. The two C-band radar systems that are considered here were unfortunately not able to provide  $\Phi_{dp}$  range measurements to extract  $K_{dp}$ . Indeed,  $K_{dp}$  may be essential not only to improve hydrometeor classification but also to provide an estimate of the total path attenuation that is very often used to estimate the specific attenuation along the storm core [8], [25], [26]. In order to correct for PIA, we can exploit the radar network configuration that is able to detect this rain event from two (or more) point of views, by either using a composite field approach or a constrained inversion algorithm [25], [26]. The approach described here may be

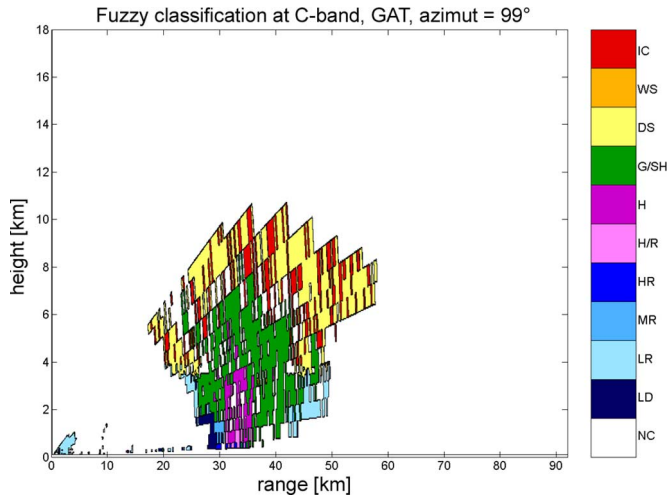


Fig. 6. Same as in Fig. 4, but using data from the GAT radar.

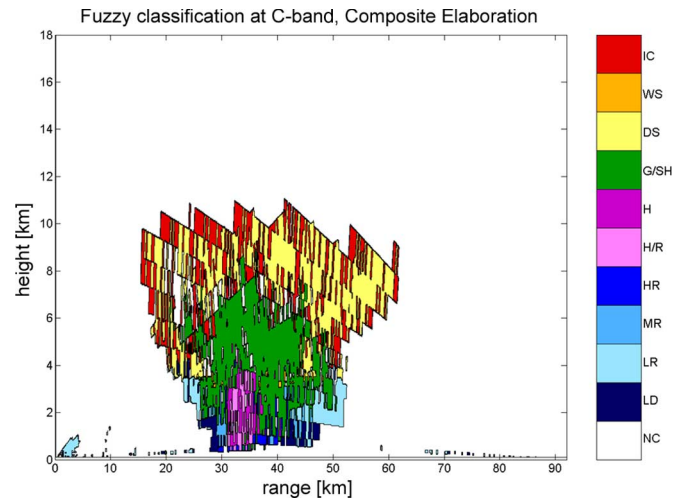


Fig. 7. Same as in Fig. 4 but applied to the composite radar reflectivity RHI, that was derived from SPC and GAT radar data.

easily extended to any radar network configuration where even single-polarization radars are present.

#### A. Composite Field Approach From a Radar Network

A composite maximum-reflectivity approach consists of two steps: 1) collocating reflectivity data that were measured from the two (or more) radars in the vertical plane containing the line-of-sight and 2) choosing the maximum value within each collocated bin. In principle, it can be used to correct the whole collocated volume data for path-attenuation effects [19].

In order to attest the differences between the two radar observations, Fig. 6 provides a hydrometeor classification RHI that is similar to that in Fig. 4 but derived from the GAT radar. It is quite clear that the consistency of the two classifications are mainly dominated by G/SH, even though the regions of H/R and H are much better detected from GAT than from SPC due to their shorter range from GAT. Indicating with  $Z_{xxm}^{SPC}$  and  $Z_{xxm}^{GAT}$  the reflectivities (either copolar or differential) that were measured from the SPC and GAT radars, respectively, we can estimate the composite reflectivity  $Z_{xx}^{COM}$  as

$$\hat{Z}_{xx}^{COM}(r, \theta, \varphi) = \text{Max}_Z [Z_{xxm}^{SPC}(r, \theta, \varphi), Z_{xxm}^{GAT}(r, \theta, \varphi)] \quad (9)$$

where  $r$  is the range,  $\theta$  is the elevation angle,  $\varphi$  is the azimuth angle, the “hat” indicates reconstructed (estimated) reflectivity (in decibels referenced to zero), and  $\text{Max}_Z$  is an operator that takes the maximum with respect to  $Z_{xxm}$ .

The accuracy of (9) is expected to be worse for those range bins where both radars are crossing the precipitation cores or regions of intense rainfall. The generalization of (9) to a more complex radar network is straightforward. In order to obtain the composite RHI, a nearest neighbor resampling of the observed RHIs has been applied. The impact of the composite radar data RHI on the FRAHCC scheme is shown in Fig. 7.

The main feature in Fig. 7 is that the graupel area of the RHI is more uniform within the main core of the convective cell,

also due to the reduction of unclassified pixels. The composite gives also a complete and detailed overview of the convective cell core.

#### B. Path-Attenuation Correction From a Radar Network

When radar network observations of a storm are available, the PIA can be estimated by looking at the differences between the attenuated measured reflectivity  $Z_{hhm}$ , which was observed from the considered radar, and the nonattenuated reflectivity  $Z_{hh}$ , which was observed by the other radar at the rain-cloud edge. This approach can compensate the lack of differential phase shift measurement capability of the considered radars, as in our case [25], [26]. The differences between the two radar observations of the same event can be derived by comparing the SPC and GAT RHIs, as shown in Figs. 2 and 3. The main problem is that radar data are quite noisy and fluctuating, so that the estimate of PIA may be affected by a significant uncertainty.

Let us consider the line connecting the SPC and GAT radars at the lowest elevation angle  $\theta_0 = 0.5^\circ$ . Along this line, an average of over 2.5 km (ten range bins) gives a value of  $5 \pm 2.4$  dBZ for the radar reflectivity difference ( $Z_{hhm}^{GAT} - Z_{hhm}^{SPC}$ ) and  $7.5 \pm 1.5$  dBZ for ( $Z_{hhm}^{SPC} - Z_{hhm}^{GAT}$ ). The average value between these two estimates seems to indicate a PIA of about 6.25 dB. In order to reconstruct the equivalent reflectivity range profiles of  $Z_{hh}$  and  $Z_{dr}$ , we can apply a path-attenuation correction algorithm with PIA constraint. A set of these algorithms is illustrated in Appendix B. The problem that we need to tackle is that the estimate of PIA is uncertain, the two radars may suffer for a different miscalibration and instrumental noise, and the various correction algorithms may give different results. In this context, we have decided to perform a variational maximum-likelihood estimation of  $Z_{hh}$  and  $Z_{dr}$  by assuming a bounded variability of all the previous sources of uncertainty.

The goal of the variational approach has been to render the reconstructed reflectivity profiles, which were estimated

from SPC and GAT radar data, as close as possible along the considered range line. We have proceeded through three steps.

- 1) We have first applied path-attenuation algorithms to get a set of estimates of  $Z_{xx}^{SPC}(r|\varepsilon_{PIA}, \varepsilon_C, \varepsilon_A)$  and  $Z_{xx}^{GAT}(r|\varepsilon_{PIA}, \varepsilon_C, \varepsilon_A)$ , which were obtained by varying all sources of uncertainty. The latter ones are indicated by  $\varepsilon_{PIA}$ ,  $\varepsilon_C$ , and  $\varepsilon_A$  standing for PIA variability, calibration errors, and algorithm diversity, respectively. For both SPC and GAT profiles, PIA has been varied between 2.5 and 9 dB, the calibration has been assumed with a possible bias between 0 and 2 dB, and three correction algorithms have been applied (i.e., the attenuation-adjustment (AA), the calibration-adjustment (CA) or reflectivity-differential phase (ZPHI), and the constrained-iterative (CI) algorithms, as in Appendix B).
- 2) In order to select the optimal estimate of the corrected reflectivity profile  $Z_{xx}^{COR}(r)$ , we have minimized, with respect to all uncertainties, an error (cost) function  $E$  that is chosen as follows:

$$E(\varepsilon_{PIA}, \varepsilon_C, \varepsilon_A) = \int_{r_0}^{r_N} \left| \hat{Z}_{xx}^{GAT}(r|\varepsilon_{PIA}, \varepsilon_C, \varepsilon_A) - \hat{Z}_{xx}^{SPC}(r|\varepsilon_{PIA}, \varepsilon_C, \varepsilon_A) \right| dr \quad (10)$$

where  $r_0$  and  $r_N$  are the closest and farthest radar ranges to the GAT radar system. It is worth remarking that the global minimum of  $E$  in (9) has been found for a PIA of about 6 dB—with the three correction algorithms indicating a PIA between 5.5 and 6.5 dB—and a calibration-error bias of about 0 dB.

- 3) Finally, the reconstructed profile has been evaluated by means of the following average:

$$\hat{Z}_{xx}^{COR}(r, \theta_0, \varphi) = 0.5 \times \left[ \hat{Z}_{xx\min}^{GAT}(r, \theta_0, \varphi) + \hat{Z}_{xx\min}^{SPC}(r, \theta_0, \varphi) \right] \quad (11)$$

where  $Z_{xx\min}$  is the minimum error solution of (10).

The results of the maximum-likelihood estimation of the range profiles of  $Z_{hh}$  and  $Z_{dr}$  are shown in Fig. 8 along the SPC–GAT lowest elevation range line. In these plots, original range profiles, which are measured from SPC and GAT radars, are also shown for comparison. The reconstructed  $Z_{hh}$  profile is quite close to the composite profile, except for the core region between 31 and 36 km, where both measured reflectivities are strongly attenuated. The effect of the reconstruction of the  $Z_{dr}$  profile is quite similar.

To reinforce the previous arguments, Fig. 9 reports the superposition of the simulated data in the plane of  $Z_{hh}$  and  $Z_{dr}$ , as shown in Fig. 1 for all classes, with the measured data from the SPC and GAT radars along their line-of-sight. Measured data, after path-attenuation correction as in (10), are displayed on the same plot. It is evident how path-attenuation correction is a fairly effective remedy ensuring consistency between simulations and measurements.

Once the range profiles of  $Z_{hh}$  and  $Z_{dr}$  have been corrected, the hydrometeor classification algorithm at the C-band can be applied. Fig. 10 shows the results that were obtained by using

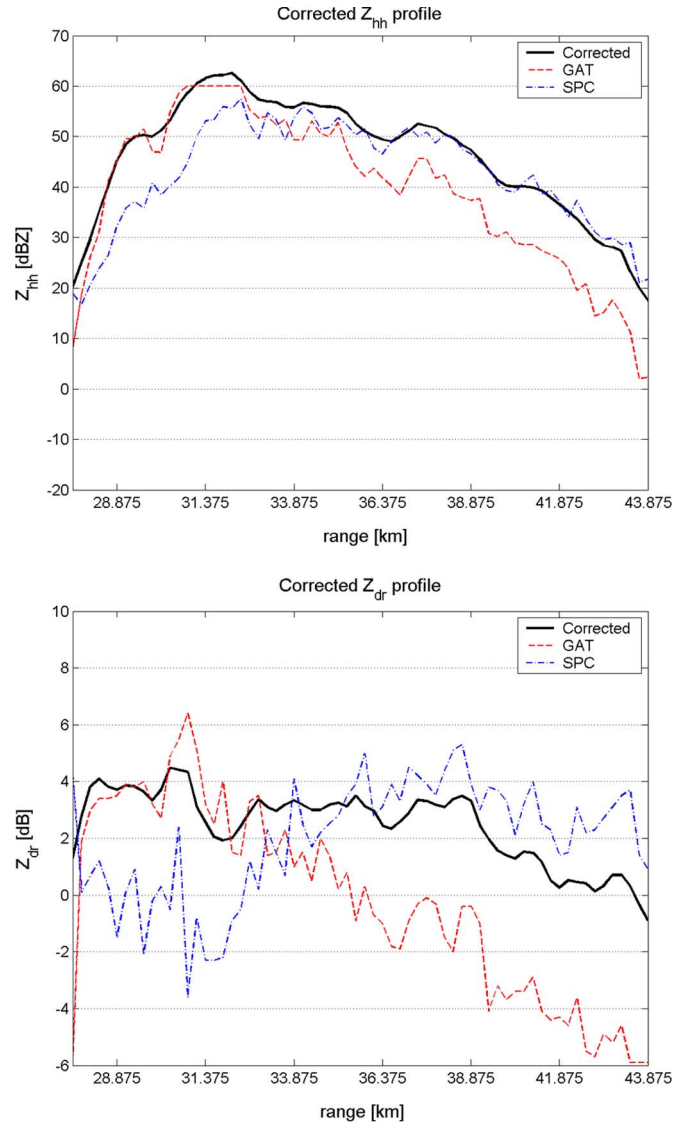


Fig. 8. Range profiles of (top panel)  $Z_{hh}$  and (bottom panel)  $Z_{dr}$  after the variational maximum-likelihood correction of rain path attenuation along the lowest elevation line connecting the SPC and GAT radars. Original profiles, which were measured from SPC and GAT radars, are also shown for comparison.

the FRAHCC technique on corrected data shown in Fig. 8. At the lowest radar elevation, we are observing the rain core. This emerges from the predominance in Fig. 10 of the LD and HR classes with some H/R on the left edge of the storm.

As a useful comparison, Fig. 11 shows the same FRAHCC classification but performed using the reflectivity profile, which was measured from the SPC radar without any path-attenuation correction. We note that path-attenuation correction tends to remove the H-class regions, provides a continuity of HR and MR, and drastically reduces the presence of LD and NC bins.

To highlight the difference between the different correction techniques and between the C-band and S-band MBFs, Fig. 12 illustrates the results that were obtained using the composite profile algorithm  $Z_{xx}^{COM}$  that was applied to the radar line GAT–SPC and using the S-band MBFs without path-attenuation correction. The use of the composite reflectivity profile, as in (9), tends to maintain the predominance of HR in the core region, even though there is an ambiguity between H/R

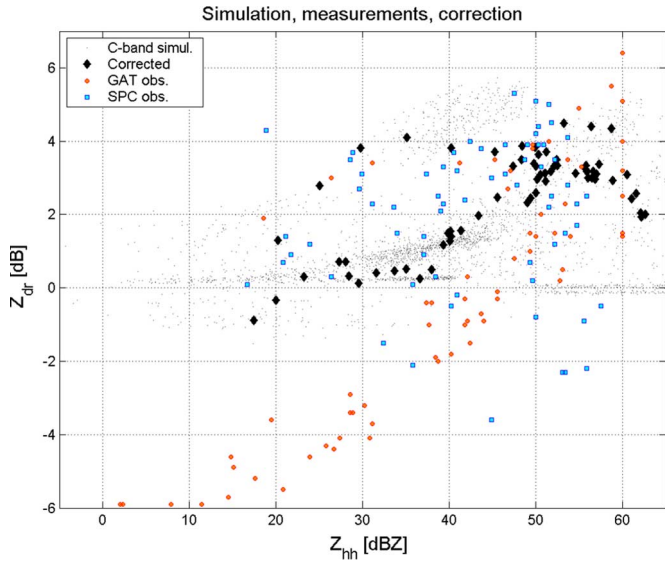


Fig. 9. Simulated  $Z_{hh}$  and  $Z_{dr}$  superimposed to measured SPC and GAT radar measurements and to path-attenuation-corrected data.

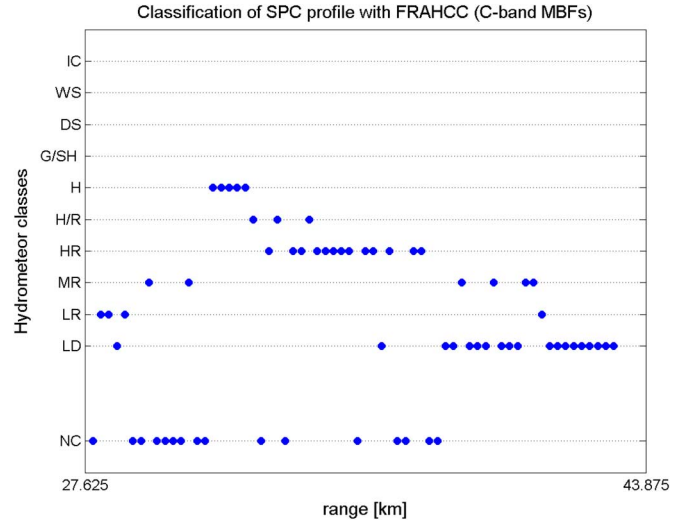


Fig. 11. Same as in Fig. 10 but using FRAHCC applied to radar data without path-attenuation correction.

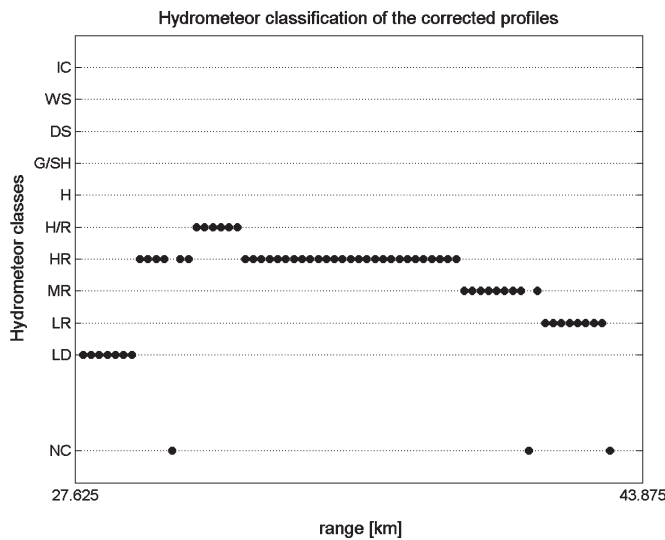


Fig. 10. Hydrometeor classification using FRAHCC, applied to line-of-sight-corrected data of Fig. 8.

and HR, and partially, between LD and MR. On the other hand, the application of the S-band MBFs tends to saturate the rain core with the LD class, showing a large amount of NC bins. The hydrometeor class rendering is highly scattered and unrealistic with respect to Fig. 11 and, particularly, to the optimal case of Fig. 10, as expected from results in Table III as well.

### VI. CONCLUSION

Backscattering radar simulations confirm the presence of noteworthy behavioral differences between S-band and C-band data. At C-band, Mie scattering resonance effects cannot be neglected, and the consequence is a major sensitivity to shapes and orientations, with respect to S-band radar responses. Using S-band MBFs to classify C-band data naturally leads to an erroneous hydrometeor classification accuracy, as revealed even by visual inspection. Making changes of fuzzy-logic MBFs is

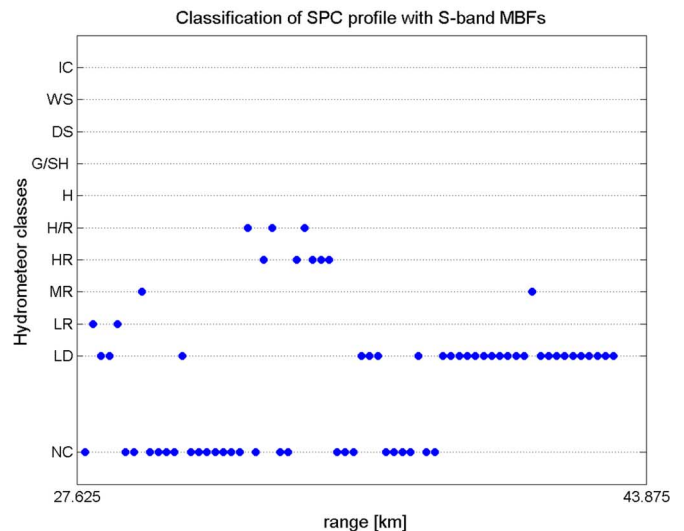
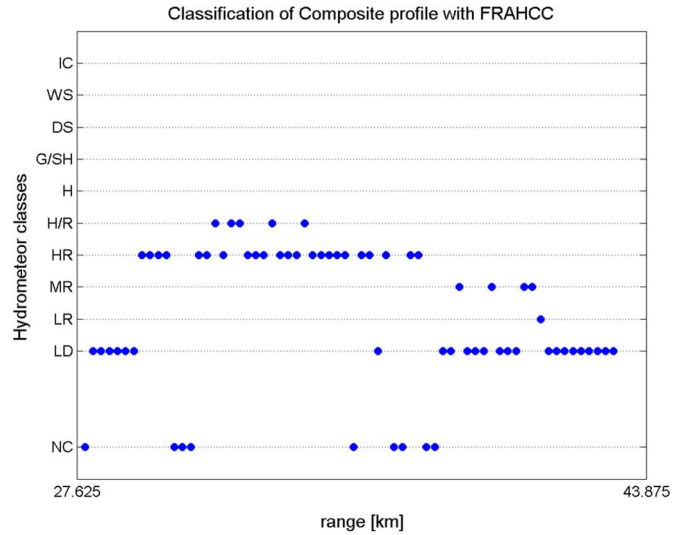


Fig. 12. Same as in Fig. 10 but using the FRAHCC algorithm applied to (top panel) the composite-data range profile and (bottom panel) using S-band MBFs without path-attenuation correction.

not straightforward: it requires solid experience and accurate observations of hydrometeor polarimetric signatures, which are derived from scattering simulations if the approach is model based. Appropriate MBFs, which are modified for C-band and constitute the basis of the FRAHCC approach, have been determined and tested on synthetic radar measurements, which were obtained by adding Gaussian noise to numerically simulated data. As a final result, the overall classification accuracy has considerably increased, and the average nonclassified bins percentage has decreased as well with respect to the use of S-band MBFs. As shown, hydrometeor classification results, using  $K_{dp}$  simulated measurements and proper MBFs, are also quite promising at C-band.

As an example, the FRAHCC technique has been applied to polar volume data sets coming from a network of two C-band radars, which are located in north Italy. The vertical section of a convective hailstorm on the line-of-sight between the two radar systems has been classified with the S-band MBF system and with the new FRAHCC system. The accuracy improvements have been directly visible by analyzing the classified RHIs: the hail core has been correctly detected, and the classification results are physically reasonable. A path-attenuation correction algorithm, based on either a composite approach or a constrained correction approach, has been also applied to the entire vertical section of the precipitating cloud. As expected, the impact on hydrometeor classification is noteworthy and tends to make the results more robust and microphysically consistent.

The outlined variational procedure for path-attenuation correction within a radar network can be extended to the entire RHI or volume radar data by considering the edge bins of the observed storm, using the near-edge reflectivity of one radar—if available, this depends on the observation geometry that should benefit from a multiple-radar network topology—as a constraint to derive the PIA for the other radar. In this case, the corrected reflectivity profile could be evaluated as the expected profile over the ensemble of possible PIA, bias, and algorithm variability, as in (10). Together with the exploitation of the information content that is carried by the C-band copolar correlation coefficient, these should be aims of future work.

#### APPENDIX A MBFs OF FRAHCC

Analytical expressions of all MBFs that were used in the FRAHCC system are reported here for completeness. In a way that is similar to [10], we introduce the trapezoidal function that is described by the following expression:  $Trap(x, a, b, s, t)$ , where  $x$  is the input value;  $a$  and  $b$  are the left and right sides of the minor base (where the function output is equal to 1, i.e., maximum membership), respectively; and  $s$  and  $t$  are the linear fuzzy thicknesses on the left and right sides, respectively. The analytical expression of the trapezoidal function  $Trap$  is

$$Trap(x, a, b, s, t) = \begin{cases} 0, & x < (a - s) \text{ or } x > (b + t) \\ (x - a + s)/s, & (a - s) \leq x \leq a \\ (b + t - x)/t, & b \leq x \leq (b + t) \\ 1, & a < x < b. \end{cases} \quad (A1)$$

Other useful functions can be defined in order to simplify MBF expressions. They are given as follows:

$$L(x) = -0.5 + 2.5 \cdot 10^{-3}x + 7.5 \cdot 10^{-4}x^2 \quad (A2)$$

$$U(x) = -0.22 + 3.64 \cdot 10^{-2}x + 3.57 \cdot 10^{-4}x^2 \quad (A3)$$

$$C_l(x) = -1.4 + 2.5 \cdot 10^{-3}x + 11.95 \cdot 10^{-4}x^2 \quad (A4)$$

$$C_u(x) = -0.22 + 2.94 \cdot 10^{-2}x + 9.66 \cdot 10^{-4}x^2 \quad (A5)$$

$$C_{ld}(x) = 1.3 + 0.138x - 6.63 \cdot 10^{-4}x^2 \quad (A6)$$

$$C_{hr}(x) = 1.65 - 0.03 \cdot x \quad (A7)$$

$$C_h(x) = -0.376 + 0.013 \cdot x. \quad (A8)$$

In the following expressions, the terms  $M_{Z_i}$  and  $M_{K_i}$  refer to a generic bidimensional MBF of the  $i$ th class and are related to the measured observables, while the term  $M_{T_i}$  refers to a monodimensional MBF that is related to  $T$ . Their combination provides the inference rules that were reported in (6) and (7).

We will introduce MBFs for amplitude backscattering observables, i.e.,  $Z_{hh}$  and  $Z_{dr}$ , and for measurable sets including the differential phase shift  $K_{dp}$ . Note that  $Z_{hh}$  is measured in decibels referenced to zero,  $Z_{dr}$  in decibels,  $K_{dp}$  in degrees per kilometer, and  $T$  in degree Celsius. The subscript in each MBF expression indicates the considered hydrometeor class: 0 stands for LD (*large drops*), 1 stands for LR (*light rain*), and so on until 9 that stands for IC (*ice crystals*).

Class 0) LD (*large drops*)

$$M_{Z_0} = Trap[Z_{hh}, 20, 45, 5, 5] \\ \cdot Trap[Z_{dr}, C_u(Z_{hh}), C_{ld}(Z_{hh}), 0.3, 0.3] \\ M_{K_0} = Trap[Z_{hh}, 20, 45, 5, 5] \\ \cdot Trap[K_{dp}, f_d(Z_{hh}), f_u(Z_{hh}), \Delta(Z_{hh}), \Delta(Z_{hh})]$$

$$M_{T_0} = \begin{cases} 0, & T < -10 \\ 0.1 \cdot T + 1, & -10 \leq T < 0 \\ 1, & T \geq 0 \end{cases}$$

$$f_d(Z_{hh}) = \begin{cases} 0, & Z_{hh} < 27 \\ 9.64 \cdot 10^{-5} \cdot Z_{hh}^3 - 0.009008 \\ \cdot Z_{hh}^2 + 0.28 \cdot Z_{hh} - 2.889, & Z_{hh} \geq 27 \end{cases}$$

$$f_u(Z_{hh}) = \begin{cases} 0.05, & Z_{hh} < 26 \\ 9.762 \cdot 10^{-5} \cdot Z_{hh}^3 - 0.009008 \\ \cdot Z_{hh}^2 + 0.283 \cdot Z_{hh} - 2.939, & Z_{hh} \geq 26 \end{cases}$$

$$\Delta(Z_{hh}) = \begin{cases} 0.1, & Z_{hh} < 30 \\ 0.01 \cdot Z_{hh} - 0.2, & Z_{hh} \geq 30. \end{cases}$$

Class 1) LR (*light rain*)

$$\begin{aligned}
 M_{Z1} &= Trap[Z_{hh}, 10, 35, 5, 5] \\
 &\quad \cdot Trap[Z_{dr}, L(Z_{hh}), C_u(Z_{hh}), 0.3, 0.3] \\
 M_{K1} &= Trap[Z_{hh}, 10, 35, 5, 5] \\
 &\quad \cdot Trap[K_{dp}, f_d(Z_{hh}), f_u(Z_{hh}), \Delta(Z_{hh}), \Delta_u(Z_{hh})] \\
 M_{T1} &= \begin{cases} 0, & T < -5 \\ 0.2 \cdot T + 1, & -5 \leq T < 0 \\ 1, & T \geq 0 \end{cases} \\
 f_d(Z_{hh}) &= \begin{cases} 0, & Z_{hh} < 30 \\ 0.003016 \cdot Z_{hh}^3 - 0.02649 \cdot Z_{hh}^2 \\ \quad + 0.7872 \cdot Z_{hh} - 7.9, & Z_{hh} \geq 30 \end{cases} \\
 f_u(Z_{hh}) &= \begin{cases} 0.05, & Z_{hh} < 27 \\ 0.000304 \cdot Z_{hh}^3 - 0.02649 \cdot Z_{hh}^2 \\ \quad + 0.7872 \cdot Z_{hh} - 7.88, & Z_{hh} \geq 27 \end{cases} \\
 \Delta(Z_{hh}) &= \begin{cases} 0.1, & Z_{hh} < 28.5 \\ 0.01 \cdot Z_{hh} - 0.2, & Z_{hh} \geq 28.5. \end{cases}
 \end{aligned}$$

Class 2) MR (*medium rain*)

$$\begin{aligned}
 M_{Z2} &= Trap[Z_{hh}, 35, 45, 5, 5] \\
 &\quad \cdot Trap[Z_{dr}, L(Z_{hh}), C_u(Z_{hh}), 0.3, 0.3] \\
 M_{K2} &= Trap[Z_{hh}, 35, 45, 5, 5] \\
 &\quad \cdot Trap[K_{dp}, f_d(Z_{hh}), f_u(Z_{hh}), \Delta(Z_{hh}), \Delta_u(Z_{hh})] \\
 M_{T2} &= \begin{cases} 0, & T < -5 \\ 0.2 \cdot T + 1, & -5 \leq T < 0 \\ 1, & T \geq 0 \end{cases} \\
 f_d(Z_{hh}) &= \begin{cases} 0, & Z_{hh} < 30 \\ 0.003016 \cdot Z_{hh}^3 - 0.02649 \cdot Z_{hh}^2 \\ \quad + 0.7872 \cdot Z_{hh} - 7.9, & Z_{hh} \geq 30 \end{cases} \\
 f_u(Z_{hh}) &= \begin{cases} 0.0003043 \cdot Z_{hh}^3 - 0.02658 \cdot Z_{hh}^2 \\ \quad + 0.7872 \cdot Z_{hh} - 7.83, & Z_{hh} < 43 \\ 0.000352 \cdot Z_{hh}^3 - 0.0286 \cdot Z_{hh}^2 \\ \quad + 0.7882 \cdot Z_{hh} - 7.88, & Z_{hh} \geq 43 \end{cases} \\
 \Delta(Z_{hh}) &= \begin{cases} 0.1, & Z_{hh} < 28.5 \\ 0.01 \cdot Z_{hh} - 0.2, & Z_{hh} \geq 28.5. \end{cases}
 \end{aligned}$$

Class 3) HR (*heavy rain*)

$$\begin{aligned}
 M_{Z3} &= Trap[Z_{hh}, 45, 60, 5, 5] \\
 &\quad \cdot Trap[Z_{dr}, C_l(Z_{hh}), C_u(Z_{hh}), 0.3, 0.3] \\
 M_{K3} &= Trap[Z_{hh}, 45, 60, 5, 5] \\
 &\quad \cdot Trap[K_{dp}, f_d(Z_{hh}), f_u(Z_{hh}), \Delta(Z_{hh}), \Delta_u(Z_{hh})] \\
 M_{T3} &= \begin{cases} 0, & T < -5 \\ 0.2 \cdot T + 1, & -5 \leq T < 0 \\ 1, & T \geq 0 \end{cases} \\
 f_d(Z_{hh}) &= \begin{cases} 0.002582 \cdot (Z_{hh} - 2.7)^3 - 0.0323 \\ \quad \cdot (Z_{hh} - 2.7)^2 + 13.6 \\ \quad \cdot (Z_{hh} - 2.7) - 191.9, & Z_{hh} < 55 \\ 1.88 \cdot Z_{hh} - 98, & Z_{hh} \geq 55 \end{cases} \\
 f_u(Z_{hh}) &= \begin{cases} 0.002612 \cdot Z_{hh}^3 - 0.3243 \cdot Z_{hh}^2 \\ \quad + 13.6 \cdot Z_{hh} - 191.6, & Z_{hh} < 53 \\ 2.479 \cdot Z_{hh} - 124, & Z_{hh} \geq 53 \end{cases} \\
 \Delta(Z_{hh}) &= 0.05 \cdot Z_{hh} - 1.7.
 \end{aligned}$$

Class 4) H/R (*hail mixed with rain*)

$$\begin{aligned}
 M_{Z4} &= Trap[Z_{hh}, 55, 75, 5, 5] \\
 &\quad \cdot Trap[Z_{dr}, C_{hr}(Z_{hh}), C_l(Z_{hh}), 0.2, 0.3] \\
 M_{K4} &= Trap[Z_{hh}, 55, 75, 5, 5] \\
 &\quad \cdot Trap[K_{dp}, f_d(Z_{hh}), f_u(Z_{hh}), \Delta_d(Z_{hh}), \Delta_u(Z_{hh})] \\
 M_{T4} &= Trap[T, 0, 20, 15, 20] \\
 f_d(Z_{hh}) &= \begin{cases} 0, & Z_{hh} < 70 \\ -0.4 \cdot Z_{hh} + 28, & Z_{hh} \geq 70 \end{cases} \\
 \Delta_d(Z_{hh}) &= \begin{cases} 0.2, & Z_{hh} < 70 \\ 0.02 + 0.08 \cdot (Z_{hh} - 70), & Z_{hh} \geq 70 \end{cases} \\
 f_u(Z_{hh}) &= 0.002582 \cdot (Z_{hh} - 7)^3 - 0.323 \cdot (Z_{hh} - 7)^2 \\
 &\quad + 13.6 \cdot (Z_{hh} - 7) - 191.9 \\
 \Delta_u(Z_{hh}) &= 0.08 \cdot (Z_{hh} - 70) + 0.1.
 \end{aligned}$$

Class 5) H (*hail*)

$$\begin{aligned}
 M_{Z5} &= Trap[Z_{hh}, 55, 75, 5, 5] \\
 &\quad \cdot Trap[Z_{dr}, -4, C_h(Z_{hh}), 0.2, 0.2] \\
 M_{K5} &= Trap[Z_{hh}, 55, 75, 5, 5] \\
 &\quad \cdot Trap[K_{dp}, f_d(Z_{hh}), f_u(Z_{hh}), \\
 &\quad \quad \quad \Delta_d(Z_{hh}), \Delta_u(Z_{hh})] \\
 M_{T5} &= Trap[T, -15, 15, 25, 25] \\
 f_d(Z_{hh}) &= \begin{cases} -1.0675, & Z_{hh} < 60 \\ -0.00126 \cdot (Z_{hh} + 5)^3 \\ \quad + 0.2336 \cdot (Z_{hh} + 5)^2 \\ \quad - 14.4 \cdot (Z_{hh} + 5) + 294, & Z_{hh} \geq 60 \end{cases} \\
 \Delta_d(Z_{hh}) &= 0.08 \cdot (Z_{hh} - 50) + 0.1 \\
 f_u(Z_{hh}) &= \begin{cases} 0.3, & Z_{hh} < 60 \\ 0.1375 \cdot Z_{hh} - 7.95, & 60 \leq Z_{hh} < 68 \\ 0.001259 \cdot (Z_{hh} + 5)^3 \\ \quad - 0.2331 \cdot (Z_{hh} + 5)^2 \\ \quad + 14.34 \cdot (Z_{hh} + 5) - 293, & Z_{hh} \geq 68 \end{cases} \\
 \Delta_u(Z_{hh}) &= 0.08 \cdot (Z_{hh} - 50) + 0.1.
 \end{aligned}$$

Class 6) G/SH (*graupel/small hail*)

$$\begin{aligned}
 M_{Z6} &= Trap[Z_{hh}, 30, 50, 5, 5] \\
 &\quad \cdot Trap[Z_{dr}, 0, L(Z_{hh}), 0.3, 0.3] \\
 M_{K6} &= Trap[Z_{hh}, 30, 50, 5, 5] \\
 &\quad \cdot Trap[K_{dp}, 0, f_u(Z_{hh}), 0.1, \Delta_u(Z_{hh})] \\
 M_{T6} &= Trap[T, -35, 0, 25, 20] \\
 f_u(Z_{hh}) &= \begin{cases} 0.05, & Z_{hh} < 33 \\ 0.0003079 \cdot (Z_{hh} - 4)^3 \\ \quad - 0.0267 \cdot (Z_{hh} - 4)^2 \\ \quad + 0.7872 \cdot (Z_{hh} - 4) - 7.83, & Z_{hh} \geq 33 \end{cases} \\
 \Delta_u(Z_{hh}) &= 0.035 \cdot (Z_{hh} - 25) + 0.1.
 \end{aligned}$$

Class 7) DS (*dry snow*)

$$\begin{aligned} M_{Z7} &= \text{Trap}[Z_{\text{hh}}, 10, 35, 7, 7] \cdot \text{Trap}[Z_{\text{dr}}, 0, 0.4, 0.3, 0.3] \\ M_{K7} &= \text{Trap}[Z_{\text{hh}}, 10, 35, 7, 7] \cdot \text{Trap}[K_{\text{dp}}, 0, 0.05, 0.1, 0.1] \\ M_{T7} &= \text{Trap}[T, -50, -1, 2, 2]. \end{aligned}$$

Class 8) WS (*wet snow*)

$$\begin{aligned} M_{Z8} &= \text{Trap}[Z_{\text{hh}}, 30, 45, 5, 5] \\ &\quad \cdot \text{Trap}[Z_{\text{dr}}, 0.5, U(Z_{\text{hh}}) + 0.5, 0.3, 0.3] \\ M_{K8} &= \text{Trap}[Z_{\text{hh}}, 30, 45, 5, 5] \\ &\quad \cdot \text{Trap}[K_{\text{dp}}, f_d(Z_{\text{hh}}), f_u(Z_{\text{hh}}), 0.1, 0.1] \\ M_{T8} &= \text{Trap}[T, -2, 2, 1, 1] \\ f_d(Z_{\text{hh}}) &= \begin{cases} 0, & Z_{\text{hh}} < 40 \\ 0.02 \cdot (Z_{\text{hh}} - 40), & Z_{\text{hh}} \geq 40 \end{cases} \\ f_u(Z_{\text{hh}}) &= 0.395 \cdot \frac{Z_{\text{hh}} - 25}{25}. \end{aligned}$$

Class 9) IC (*ice crystals*)

$$\begin{aligned} M_{Z9} &= \text{Trap}[Z_{\text{hh}}, 5, 30, 5, 5] \cdot \text{Trap}[Z_{\text{dr}}, 0.5, 2.7, 0.3, 0.3] \\ &\quad + \text{Trap}[Z_{\text{hh}}, 5, 30, 5, 5] \\ &\quad \cdot \text{Trap}[Z_{\text{dr}}, -2.7, -0.5, 0.3, 0.3] \\ M_{K9} &= \text{Trap}[Z_{\text{hh}}, 5, 30, 5, 5] \\ &\quad \cdot \text{Trap}[K_{\text{dp}}, -0.05, 0.05, 0.1, 0.1] \\ M_{T9} &= \text{Trap}[T, -70, -8, 5, 5]. \end{aligned}$$

## APPENDIX B

## PATH-ATTENUATION CORRECTION ALGORITHMS

The family of the considered path-attenuation correction algorithms is briefly summarized here. We will refer to copolar reflectivity  $Z_{\text{hh}}$  (in  $\text{mm}^6 \cdot \text{m}^{-3}$ ) as the extension to  $Z_{\text{vv}}$  is straightforward. Measured copolar reflectivity  $Z_{\text{hhm}}$  is related to equivalent reflectivity  $Z_{\text{hh}}$  and specific attenuation  $A_{\text{hh}}$  by (1). If  $r_N$  is the farthest range bin (i.e., the edge of either the rain-cell or the selected range interval), the copolar path-attenuation factor  $L_{\text{hh}}$  can be evaluated from PIA by

$$\begin{aligned} L_{\text{hh}} &= \frac{Z_{\text{hhm}}(r_N)}{Z_{\text{hh}}(r_N)} = e^{-0.46 \int_{r_0}^{r_N} A_{\text{hh}}(r') dr'} \\ &= 10^{-0.1 \cdot 2 \cdot \text{PIA}_{\text{hh}}(r_0, r_N)}. \end{aligned} \quad (\text{B1})$$

Following Iguchi and Meneghini [23] and assuming a power-law relation between specific attenuation  $A_{\text{hh}}$  (in decibels per kilometer) and copolar reflectivity  $Z_{\text{hh}}$

$$A_{\text{hh}} = a Z_{\text{hh}}^b \quad (\text{B2})$$

with, for example,  $a = 0.19 \cdot 10^{-4}$  and  $b = 0.826$  at C-band for temperatures between 0 °C and 40 °C; the AA solution to (1), which is also called alpha adjustment in [23], with the constraint (B1), is given by

$$\hat{Z}_{\text{hh}}^{(\text{AA})}(r) = \frac{Z_{\text{hhm}}(r) [I_{\text{hh}}(r_0, r_N)]^{1/b}}{[I_{\text{hh}}(r_0, r_N) - (1 - L_{\text{hh}}^b) I_{\text{hh}}(r_0, r)]^{1/b}} \quad (\text{B3})$$

where the integral  $I_{\text{hh}}$  is given by

$$I_{\text{hh}}(r_0, r) = 0.46b \int_{r_0}^r Z_{\text{hhm}}^b(r') dr'. \quad (\text{B4})$$

On the other hand, the CA solution to (1), which is also called constant adjustment in [23], is given by

$$\hat{Z}_{\text{hh}}^{(\text{CA})}(r) = \frac{(1 - L_{\text{hh}}^b)^{1/b} Z_{\text{hhm}}(r)}{a^{1/b} \{I_{\text{hh}}(r_0, r_N) - (1 - L_{\text{hh}}^b) I_{\text{hh}}(r_0, r)\}^{1/b}}. \quad (\text{B5})$$

It is worth noting that (B5) is formally equivalent to the ZPHI solution once the PIA (and then  $L_{\text{hh}}$ ) is estimated via  $\Phi_{\text{dp}}$  [25].

The third considered approach is the class of CI algorithms. Expressing  $Z_{\text{hh}}$  in decibels referenced to zero and with  $\Delta r$  as the range bin resolution, the following backward recursive equations hold for  $i = N$  to 0:

$$\hat{Z}_{\text{hh}}^{(\text{CI})}(r_N) = Z_{\text{hhm}}(r_N) + 2\text{PIA}_{\text{hh}}(r_N) \quad (\text{B6})$$

$$\text{PIA}_{\text{hh}}(r_{N-1}) = \text{PIA}_{\text{hh}}(r_N) - \hat{A}_{\text{hh}}(r_N) \cdot \Delta r \quad (\text{B7})$$

$$\hat{Z}_{\text{hh}}^{(\text{CI})}(r_{N-1}) = Z_{\text{hhm}}(r_{N-1}) + 2\text{PIA}_{\text{hh}}(r_{N-1}) \quad (\text{B8})$$

where  $A_{\text{hh}}$  is estimated by means of

$$\hat{A}(r_i) = F[Z_{\text{hh}}(r_i), Z_{\text{dr}}(r_i)] \quad (\text{B9})$$

with  $r_i$  being the discretized range and  $F$  being either a feedforward neural-network estimator [26] or a polynomial piecewise regression operator on  $Z_{\text{hh}}$  only, as in this paper.

## ACKNOWLEDGMENT

The authors would like to thank Dr. M. Celano and Dr. P. P. Alberoni (ARPA-SIM, Bologna, Italy) for providing radar data and for their helpful suggestions.

## REFERENCES

- [1] M. P. M. Hall, J. W. F. Goddard, and S. M. Cherry, "Identification of hydrometeors and other targets by dual-polarization radar," *Radio Sci.*, vol. 19, no. 1, pp. 132–140, 1984.
- [2] V. N. Bringi, R. M. Rasmussen, and J. Vivekanandan, "Multiparameter radar measurements in Colorado convective storms—Part I: Graupel melting studies," *J. Atmos. Sci.*, vol. 43, no. 22, pp. 2245–2563, Nov. 1986.
- [3] K. Aydin, Y. Zhao, and T. A. Seliga, "A differential reflectivity radar hail measurements technique: Observations during the Denver hailstorm of 13 June 1984," *J. Atmos. Ocean. Technol.*, vol. 7, no. 1, pp. 104–113, Feb. 1990.
- [4] D. S. Zrnica, V. N. Bringi, N. Balakrishnan, K. Aydin, V. Chandrasekar, and J. Hubbert, "Polarimetric measurements in a severe hailstorm," *Mon. Weather Rev.*, vol. 121, no. 8, pp. 2223–2238, Aug. 1993.
- [5] D. S. Zrnica and A. V. Ryzhkov, "Advantages of rain measurements using specific differential phase," *J. Atmos. Ocean. Technol.*, vol. 13, no. 2, pp. 454–464, Apr. 1996.
- [6] J. Vivekanandan, D. S. Zrnica, S. M. Ellis, R. Oye, A. V. Ryzhkov, and J. Straka, "Cloud microphysics retrieval using S-band dual-polarization radar measurements," *Bull. Amer. Meteorol. Soc.*, vol. 80, no. 3, pp. 381–388, Mar. 1999.
- [7] J. M. Straka, D. S. Zrnica, and A. V. Ryzhkov, "Bulk hydrometeor classification and quantification using polarimetric radar data: Synthesis of relations," *J. Appl. Meteorol.*, vol. 39, no. 8, pp. 1341–1372, Aug. 2000.
- [8] V. N. Bringi and V. Chandrasekar, *Polarimetric Doppler Weather Radar*. Boston, MA: Cambridge Univ. Press, 2001.

- [9] H. Liu and V. Chandrasekar, "Classification of hydrometeors based on polarimetric radar measurements: Development of fuzzy logic and neuro-fuzzy systems, and in situ verification," *J. Atmos. Ocean. Technol.*, vol. 17, no. 2, pp. 140–164, Feb. 2000.
- [10] D. S. Zrnica, A. V. Ryzhkov, J. Straka, Y. Liu, and J. Vivekanandan, "Testing a procedure for automatic classification of hydrometeor types," *J. Atmos. Ocean. Technol.*, vol. 18, no. 6, pp. 892–913, Jun. 2001.
- [11] S. Lim, V. Chandrasekar, and V. N. Bringi, "Hydrometeor classification system using dual-polarization radar measurements: Model improvements and in situ verification," *IEEE Trans. Geosci. Remote Sens.*, vol. 43, no. 4, pp. 792–801, Apr. 2005.
- [12] A. V. Ryzhkov, T. J. Schuur, D. W. Burgess, P. L. Heinselman, S. E. Giangrande, and D. S. Zrnica, "The joint polarization experiment: Polarimetric rainfall measurements and hydrometeor classification," *Bull. Amer. Meteorol. Soc.*, vol. 86, no. 6, pp. 809–824, Jun. 2005.
- [13] D. S. Zrnica, T. D. Keenan, L. D. Carey, and P. May, "Sensitivity analysis of polarimetric variables at a 5-cm wavelength in rain," *J. Appl. Meteorol.*, vol. 39, no. 9, pp. 1514–1526, Sep. 2000.
- [14] A. V. Ryzhkov and D. S. Zrnica, "Radar polarimetry at S, C and X bands comparative analysis and operational implications," in *Proc. 32nd Conf. Radar Meteorol.*, 2005, n. 9R3.
- [15] P. W. Barber and C. Yeh, "Scattering of electromagnetic waves by arbitrarily shaped dielectric bodies," *Appl. Opt.*, vol. 14, no. 12, pp. 2864–2872, Dec. 1975.
- [16] P. P. Alberoni, D. S. Zrnica, A. V. Ryzhkov, and L. Guerrieri, "Use of a fuzzy logic classification scheme with a C-band polarimetric radar: First results," in *Proc. ERAD*, 2002, pp. 324–327.
- [17] T. D. Keenan, "Hydrometeor classification with a C-band polarimetric radar," *Aust. Meteorol. Mag.*, vol. 52, no. 1, pp. 23–31, 2003.
- [18] L. Baldini, E. Gorgucci, and V. Chandrasekar, "Hydrometeor classification methodology for C-band polarimetric radars," in *Proc. ERAD*, 2004, pp. 62–66.
- [19] M. Galletti, P. P. Alberoni, V. Levizzani, and M. Celano, "Assessment and tuning of the behaviour of a microphysical characterisation scheme," *Adv. Geosci.*, vol. 2, pp. 145–150, 2005.
- [20] J. J. Gourley, P. Tabary, and J. Parent du Chatelet, "Classification of hydrometeors and non-hydrometeors using polarimetric C-band radar," in *Proc. 32nd Conf. Radar Meteorol.*, 2005, n. 11R4.
- [21] F. S. Marzano, D. Scaranari, M. Celano, P. P. Alberoni, G. Vulpiani, and M. Montopoli, "Hydrometeor classification from dual-polarized weather radar: Extending fuzzy logic from S-band to C-band data," *Adv. Geosci.*, vol. 7, pp. 109–114, 2006.
- [22] P. P. Alberoni, L. Ferraris, F. S. Marzano, S. Nanni, R. Pelosini, and F. Siccardi, "The Italian radar network: Current status and future developments," in *Proc. ERAD*, 2002, pp. 339–344.
- [23] T. Iguchi and R. Meneghini, "Intercomparison of single-frequency methods for retrieving a vertical rain profile from airborne or spaceborne radar data," *J. Atmos. Ocean. Technol.*, vol. 11, no. 12, pp. 1507–1516, 1994.
- [24] F. S. Marzano, L. Roberti, S. Di Michele, A. Tassa, and A. Mugnai, "Modeling of apparent radar reflectivity due to convective clouds at attenuating wavelengths," *Radio Sci.*, vol. 38, no. 1, 1002, 2003. DOI: 10.1029/2002RS002613.
- [25] J. Testud, E. Le Bouar, E. Obligis, and M. Ali-Mehenni, "The rain profiling algorithm applied to polarimetric weather radar," *J. Atmos. Ocean. Technol.*, vol. 17, no. 3, pp. 332–356, Mar. 2000.
- [26] G. Vulpiani, F. S. Marzano, V. Chandrasekar, and S. Lim, "Constrained iterative technique with embedded neural-network for dual-polarization radar correction of rain path attenuation," *IEEE Trans. Geosci. Remote Sens.*, vol. 43, no. 10, pp. 2305–2314, Oct. 2005.
- [27] M. I. Mishchenko and L. D. Travis, "Capabilities and limitations of a current Fortran implementation of the T-matrix method for randomly oriented, rotationally symmetric scatterers," *J. Quant. Spectrosc. Radiat. Transf.*, vol. 60, no. 3, pp. 309–324, 1998.
- [28] P. S. Ray, "Broadband complex refractive indices of ice and water," *Appl. Opt.*, vol. 11, no. 8, pp. 1836–1844, Aug. 1972.
- [29] D. Atlas and C. W. Ulbrich, "Path- and area-integrated rainfall measurement by microwave attenuation in 1–3 cm band," *J. Appl. Meteorol.*, vol. 16, no. 12, pp. 1322–1331, Dec. 1977.
- [30] K. V. Beard and D. Chuang, "A new model for the equilibrium shape of raindrops," *J. Atmos. Sci.*, vol. 44, no. 11, pp. 1509–1524, Jun. 1987.
- [31] S. G. Warren, "Optical constants of ice from the ultraviolet to the microwave," *Appl. Opt.*, vol. 23, no. 8, pp. 1206–1225, Apr. 1984.
- [32] R. S. Sekhon and R. C. Srivastava, "Snow size spectra and radar reflectivity," *J. Atmos. Sci.*, vol. 27, no. 2, pp. 299–307, Mar. 1970.
- [33] J. M. Mendel, "Fuzzy logic systems for engineering: A tutorial," *Proc. IEEE*, vol. 83, no. 3, pp. 345–377, Mar. 1995.
- [34] T. M. Lillesand and R. W. Kiefer, *Remote Sensing and Image Interpretation*, 3rd ed. Hoboken, NJ: Wiley, 1994.
- [35] P. P. Alberoni, T. Andersson, P. Mezzasalma, D. B. Michelson, and S. Nanni, "Use of the vertical reflectivity profile for identification of anomalous propagation," *Meteorol. Appl.*, vol. 8, no. 3, pp. 257–266, 2001.
- [36] T. S. Glickman, Ed., *AMS Glossary of Meteorology*, 2nd ed. Lawrence, KS: Amer. Meteorol. Soc., 2000.
- [37] D. Hudak, P. Rodriguez, G. W. Lee, A. Ryzhkov, F. Fabry, and N. Donaldson, "Winter precipitation studies with a dual polarized C-band radar," in *Proc. ERAD*, Sep. 18–23, 2006, pp. 300–303. Barcelona (E).



**Frank Silvio Marzano** (S'89–M'99–SM'03) received the Laurea degree (*cum laude*) in electrical engineering and the Ph.D. degree in applied electromagnetics from the University of Rome "La Sapienza," Rome, Italy, in 1988 and 1993, respectively.

In 1993, he collaborated with the Institute of Atmospheric Physics, National Research Council (CNR), Rome. From 1994 to 1996, he was with the Italian Space Agency, Rome, as a Postdoctorate Researcher. After working as a Lecturer with the University of Perugia, Perugia, Italy, in 1997, he joined the Department of Electrical Engineering and cofounded the Center of Excellence (CETEMPS), University of L'Aquila, L'Aquila, Italy, coordinating the Satellite and Radar Remote Sensing Laboratory. In 2005, he joined the Department of Electronic Engineering, University of Rome "La Sapienza," where he currently teaches courses on antennas, propagation, and remote sensing. His current research interests include passive and active remote sensing of the atmosphere from ground-based, airborne, and spaceborne platforms, particularly focusing on precipitation using microwave and infrared data, development of inversion methods, radiative transfer modeling of scattering media, and radar meteorology issues. He is also involved in radiopropagation topics in relation to incoherent wave modeling, scintillation prediction, and rain fading analysis along satellite microwave links.

Dr. Marzano was the recipient of the Young Scientist Award of the XXIV URSI General Assembly in 1993 and the ARPAD award from NRL Washington, DC, in 1998. Since 2001, he has been the Italian National Delegate for the European COST actions 720 and 280. Since January 2004, he has been an Associate Editor of the IEEE GEOSCIENCE AND REMOTE SENSING LETTERS.



**Daniele Scaranari** received the Laurea degree in electronic engineering (*cum laude*) and the post-lauream Master's degree in satellites and orbiting platforms from the University of Rome "La Sapienza," Rome, Italy, in 2005 and 2006, respectively.

He then joined the Department of Electronic Engineering, University of Rome "La Sapienza," to cooperate on radar remote sensing of rainfall. Since November 2006 he has been with Sofiter System Engineering as technical advisor within the Observation Systems and Radars Business Unit, Thales Alenia Space, Rome.



**Gianfranco Vulpiani** (M'03) received the Laurea degree in physics and the Ph.D. degree in radar meteorology from the University of L'Aquila, L'Aquila, Italy, in 2001 and 2005, respectively.

In 2001, he joined the Department of Physics and the Center of Excellence (CETEMPS) as a Research Scientist on ground-based radar meteorology, with special focus on C-band applications and polarimetric applications. In 2004, he was a Visiting Scientist with Colorado State University, Fort Collins. In February 2006, he joined the Radar Research Group, Météo France, Trappes, France. He is a reviewer for several international journals in remote sensing topics.